JGR Oceans

RESEARCH ARTICLE

Key Points:
- Autonomous piloted and Lagrangian drifting platforms measured air-sea properties and fluxes in the northwestern tropical Atlantic
- Sensible heat, latent heat, and upward buoyancy flux varied by as much as 10, 50, and 10 Wm^{-2} across 10–100 km sea surface temperature (SST) gradients
- Spatial SST gradients were a leading cause of sensible heat flux variability, but humidity fluctuations largely modulated latent heat flux

Correspondence to:
S. Iyer,
iyersu@oregonstate.edu

Small-Scale Spatial Variations of Air-Sea Heat, Moisture, and Buoyancy Fluxes in the Tropical Trade Winds

Suneil Iyer[1,2] , **Kyla Drushka[1,2]** , **Elizabeth J. Thompson[3]** , and **Jim Thomson[1]**

[1]Applied Physics Laboratory, University of Washington, Seattle, WA, USA, [2]School of Oceanography, University of Washington, Seattle, WA, USA, [3]NOAA Physical Sciences Laboratory, Boulder, CO, USA

Abstract Observations from two autonomous Wave Gliders and six Lagrangian Surface Wave Instrument Float with Tracking drifters in the northwestern tropical Atlantic during the January–February 2020 NOAA Atlantic Tradewind Ocean-atmosphere Mesoscale Interaction Campaign (ATOMIC) are used to evaluate the spatial variability of bulk air-sea heat, moisture, and buoyancy fluxes. Sea surface temperature (SST) gradients up to 0.7°C across 10–100 km frequently persisted for several days. SST gradients were a leading cause of systematic spatial air-sea sensible heat flux gradients, as variations over 5 Wm^{-2} across under 20 km were observed. Wind speed gradients played no significant role and air temperature adjustments to SST gradients sometimes acted to reduce spatial flux gradients. Wind speed, air temperature, and air humidity caused high-frequency spatial and temporal flux variations on both sides of SST gradients. A synthesis of observations demonstrated that fluxes were usually enhanced on the warm SST side of gradients compared to the cold SST side, with variations up to 10 Wm^{-2} in sensible heat and upward buoyancy fluxes and 50 Wm^{-2} in latent heat flux. Persistent SST gradients and high-frequency air temperature variations each contributed up to 5 Wm^{-2} variability in sensible heat flux. Latent heat flux was instead mostly driven by air humidity variability. Atmospheric gradients may result from convective structures or high-frequency turbulent fluctuations. Comparisons with 0.05°-resolution daily satellite SST observations demonstrate that remote sensing observations or lower-resolution models may not capture the small-scale spatial ocean variability present in the Atlantic trade wind region.

Plain Language Summary Two autonomously piloted Wave Gliders and six surface current-following drifters were deployed in the northwestern tropical Atlantic during the January–February 2020 NOAA Atlantic Tradewind Ocean-atmosphere Mesoscale Interaction Campaign to study how air-sea interaction varies on small spatial scales. The observations show that sea surface temperature (SST) can vary by up to 0.7°C over tens of kilometers of distance and that these SST fronts often persisted for several days. Larger fluxes of heat, moisture, and buoyancy typically occurred between the atmosphere and the ocean on the warm sides of SST fronts. The spatial variations of air-sea fluxes across tens of kilometers are important because these small scales are not resolved in many prediction models or satellite-based products. Thus, this work emphasizes the physics of, and importance of considering, persistent small-scale gradients in SST and air-sea fluxes in regional and global analyses.

1. Introduction

1.1. Importance and Previous Studies

Fluxes of heat, moisture, and buoyancy between the ocean and atmosphere modulate synoptic to global-scale weather and climate. Despite this importance, uncertainty remains in our understanding of how air-sea fluxes vary across small spatial scales, which are difficult to observe remotely. Much of the existing research on the atmospheric response to spatial ocean variability has utilized satellite observations to assess the influence of ocean mesoscale features on scales of 25 to hundreds of kilometers (e.g., Chelton & Xie, 2010; Chelton et al., 2004; Gaube et al., 2015; O'Neill et al., 2005; R. Small et al., 2008). In short, these studies have shown that sea surface temperature (SST) and air humidity gradients across mesoscale features lead to gradients in air-sea heat and momentum fluxes, which modify atmospheric dynamics. For example, heating over the warm side of an SST front destabilizes the atmospheric boundary layer, increasing surface wind speeds through either downward momentum transfer (Wallace et al., 1989) or pressure differences (Lindzen & Nigam, 1987). These SST-driven processes have been shown to induce atmospheric convergence and thus encourage atmospheric convection.

Bulk air-sea sensible and latent heat fluxes are typically defined as functions of the SST, air temperature, air humidity, air density, and wind speed (Fairall, Bradley, Rogers, et al., 1996; Fairall et al., 2003), while the air-sea buoyancy flux into the atmosphere is a weighted sum of both the sensible and latent heat fluxes (Stull, 1988). Thus, spatial variations in ocean properties including SST, stratification, and surface wind stress are expected to create spatial variability in air-sea heat, moisture, and buoyancy fluxes. Flux gradients have been shown in large-scale model analyses (Bishop et al., 2017; R. J. Small et al., 2019) on a range of spatial scales and have been observed near eddies, fronts, and boundary currents (e.g., Businger & Shaw, 1984; Kelly et al., 2010; Kwon et al., 2010; Minobe et al., 2008; R. Small et al., 2008; Sweet et al., 1981), including across strong surface current gradients in the subtropical ocean (Friehe et al., 1991; Seo, 2017; Shao et al., 2019) and tropical instability waves in the equatorial ocean (Hayes et al., 1989; Seo et al., 2007; Thum et al., 2002; Zhang & McPhaden, 1995).

High-resolution model simulations suggest that SST fronts can influence the dynamics of the atmospheric boundary layer across small horizontal spatial scales of hundreds of meters to 10 km (Lambaerts et al., 2013; Redelsperger et al., 2019; Samelson et al., 2006, 2020; Strobach et al., 2022; Sullivan et al., 2020, 2021; Wenegrat & Arthur, 2018) through changes in air-sea heat fluxes: increases or decreases in the sensible and latent heat fluxes on the warm or cold side of a SST front, respectively, influence the upward buoyancy flux into the atmosphere. The net effect is that increased turbulence and deeper atmospheric boundary layers would be expected on the warm sides of fronts (Samelson et al., 2006) as a result of greater vertical velocities and their variances. Increased sensible and latent heat fluxes can also lead to greater low-level atmospheric instability through warming and moistening the lowest level of the atmosphere. The atmospheric response to ocean gradients is also dependent on the relative alignment of the wind and SST front (Samelson et al., 2020; Sullivan et al., 2020, 2021). Unlike with SST gradients on scales of hundreds of kilometers, the atmosphere does not fully equilibrate to smaller-scale spatial variations in heat fluxes (R. J. Small et al., 2019) and thus small-scale ocean features can generate persistent spatial variability in air-sea fluxes, which has been hypothesized to influence local atmospheric convection and weather patterns (e.g., Redelsperger et al., 2019; Strobach et al., 2022).

The present study will focus on the trade wind region of the tropical Atlantic (Figure 1), where extensive research in the context of spatial variability has not been done. The trade wind region is characterized by near-constant winds, ocean currents that either follow the wind and waves or counter them due to submesoscale features (Iyer et al., 2022), and relatively weak SST frontal activity (Figure 1 of Mauzole, 2022). We evaluate the effects of spatial variations of SST and atmospheric parameters on fluxes at scales of tens of kilometers to provide observational evidence that smaller-scale features may influence atmospheric convection and dynamics. This can also be the case away from regions with coherent ocean mesoscale activity.

Global and regional climate models that resolve mesoscale ocean features show a stronger influence of ocean variability on air-sea interaction (Laurindo et al., 2022) and have reduced biases compared to lower-resolution models (Bryan et al., 2010; R. J. Small et al., 2014; Su et al., 2018), including in the tropical Atlantic (Seo et al., 2006). This further suggests submeso-to mesoscale ocean features play a role in the global coupled climate system. Widely-utilized satellite air-sea flux products differ as a result of different retrieval methods for components of the fluxes, different spatial and temporal resolution, and differences in the bulk parameterizations used (Table 1 of Yu, 2019). A secondary objective of the present study is to gain insight into the uncertainty in lower-resolution applications, which resolve air-sea heat, moisture, and buoyancy fluxes on relatively large scales, in trade wind regions. To this end, we make comparisons between high-resolution in situ bulk flux observations and fluxes estimated from a composite satellite SST product.

2. Data

2.1. Study Site and Satellite Data

The NOAA Atlantic Tradewind Ocean-atmosphere Mesoscale Interaction Campaign (ATOMIC), part of EUREC[4]A (Stevens et al., 2021), took place in the trade wind region of the northwest tropical Atlantic in January–February 2020 (Figure 1). Quinn et al. (2021) present a detailed synopsis of the ATOMIC ship and autonomous platform instruments used in the field campaign, which included various instrument deployments and two cruise legs on the NOAA Ship *Ronald H. Brown*. Moderate ocean current (Iyer et al., 2022) and SST variability exists on spatial scales of tens of kilometers (Figures 1 and 2), ultimately resulting from mesoscale activity associated with North Brazil Current eddies (Ffield, 2005; Fratantoni & Glickson, 2002; Fratantoni &
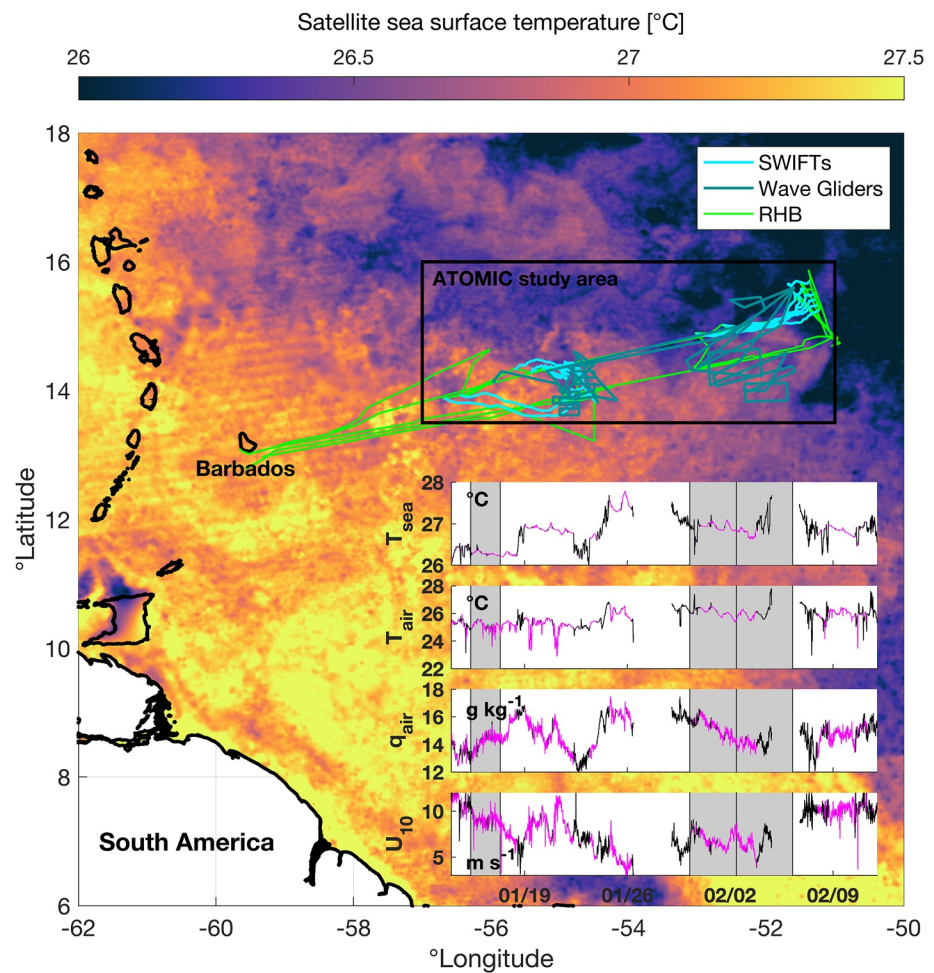
Figure 1. Group for High Resolution Sea Surface Temperature (GHRSST)-Operational Sea Surface Temperature and Sea Ice Analysis (OSTIA) satellite Sea surface temperature (SST) at 09:00 UTC on 3 February 2020 near the Atlantic Tradewind Ocean-atmosphere Mesoscale Interaction Campaign (ATOMIC) study area. Cyan, blue-green, and bright green lines denote Surface Wave Instrument Float with Tracking (SWIFT), Wave Glider, and NOAA Ship *Ronald H. Brown* tracks during ATOMIC. Inset plots show time series of SST, air temperature, air specific humidity, and wind speed from the *Ronald H. Brown* when the ship was moving (black) or stationary (pink; speed over ground <0.5 ms^{-1}). Gray shading denotes the times of three case studies highlighted in the manuscript.

Richardson, 2006), the cascade of mesoscale to submesoscale energy (e.g., Capet et al., 2008), and, in boreal spring through fall, river outflow from the South American continent. The observed distribution of relatively warm and cold water (Figures 1 and 2) resulted in conditions where prevailing trade winds blew across the large-scale northwest-southeast aligned SST gradients and fronts.

In the following sections, SWIFT and Wave Glider observations are compared to SST from a composite satellite product, the Group for High Resolution Sea Surface Temperature (GHRSST) Level 4 Operational Sea Surface Temperature and Sea Ice Analysis (OSTIA) Global Foundation Sea Surface Temperature Analysis (UK Met Office, 2005). This product is consistent with observations near the study site with a small (on the order of 0.1°C) varying regional bias (Wick et al., 2022).

2.2. SWIFT Observations

Surface Wave Instrument Float with Tracking (SWIFT) drifters are nearly Lagrangian surface-following platforms (Thomson, 2012) with a minimal amount of windage (Iyer et al., 2022). Two version 3 (v3) SWIFT drifters (Thomson, 2012) and four version 4 (v4) SWIFT drifters (Thomson et al., 2019) were deployed as part of the
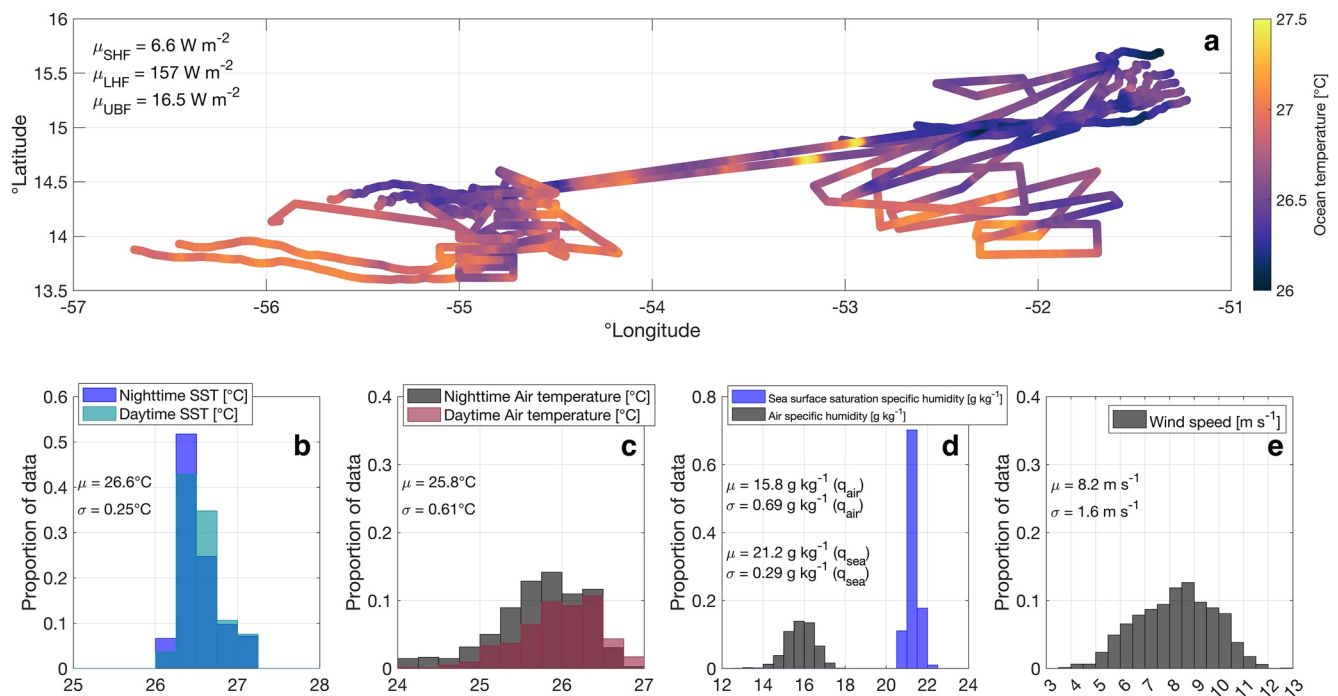
Figure 2. Surface Wave Instrument Float with Tracking (SWIFT) observations from 14 January 2020 to 11 February 2020 during Atlantic Tradewind Ocean-atmosphere Mesoscale Interaction Campaign (ATOMIC) (a) Map of sea surface temperature (SST) (observed at 0.3 m depth) (b) Histograms of nighttime and daytime SST (c) Histograms of nighttime and daytime 0.5 m air temperatures (d) 0.5 m air specific humidity and ocean surface saturation specific humidity (e) Wind speed corrected to 10 m height.

ATOMIC field campaign from the NOAA Ship *Ronald H. Brown* from 14 January 2020 to 22 January 2020 and 30 January 2020 to 11 February 2020 (Figure 1). The present study will only analyze observations from v4 drifters, which were equipped with Vaisala 350WX meteorological sensors at 0.5 m height and Aanderaa 4319 conductivity-temperature sensors at 0.3 m depth and thus made the observations necessary to calculate bulk air-sea heat, moisture, and buoyancy fluxes. We will refer to the v4 platforms simply as SWIFTs hereinafter in this manuscript. As minimal near-surface stratification was present, ocean temperature measured at 0.3 m depth is taken as SST. The mean cool skin correction (Fairall, Bradley, Godfrey, et al., 1996; Paulson & Simpson, 1981) calculated at the *Ronald H. Brown* was 0.2°C and is applied when calculating bulk air-sea fluxes. Downwelling radiation was not measured to estimate the skin SST locally using a bulk cool-skin algorithm (Fairall, Bradley, Rogers, et al., 1996). SWIFTs were also equipped with a GPS, Nortek Signature 1000 ADCPs to measure near-surface currents, and an SBG Ellipse attitude and heading reference system to measure wave parameters and spectra. Instrumentation, deployment strategy, and additional background on SWIFT drifters is described in detail by Iyer et al. (2022). All SWIFT data shown in the present study are 10-min averages from the top of each hour sent via Iridium telemetry.

2.3. Wave Glider Observations

Two Liquid Robotics Wave Gliders (Hine et al., 2009) were deployed during ATOMIC on 9 January 2020. One of the Wave Gliders was recovered on 7 February 2020 (30 days deployed) and the other was recovered on 11 February 2020 (34 days). Wave Gliders were equipped with GPS and sensors at several heights and depths used to measure atmospheric and oceanic parameters (Quinn et al., 2021). The present study will utilize atmospheric observations at 1.3 m height from Airmar WX200 meteorological sensors, which measured wind speed as well as air temperature and pressure, in addition to observations from Aanderaa 4319 sensors, which measured ocean temperature and conductivity at 0.24 m depth. The 0.24 m ocean temperature measurements from the Wave Gliders will hereinafter be referred to as SST. As with the SWIFT measurements, downwelling radiation was not measured so local skin SST estimates could not be made. Wave Gliders were also equipped with Vaisala WXT530 meteorological sensors at 1.0 m height, which measured the above atmospheric parameters in addition
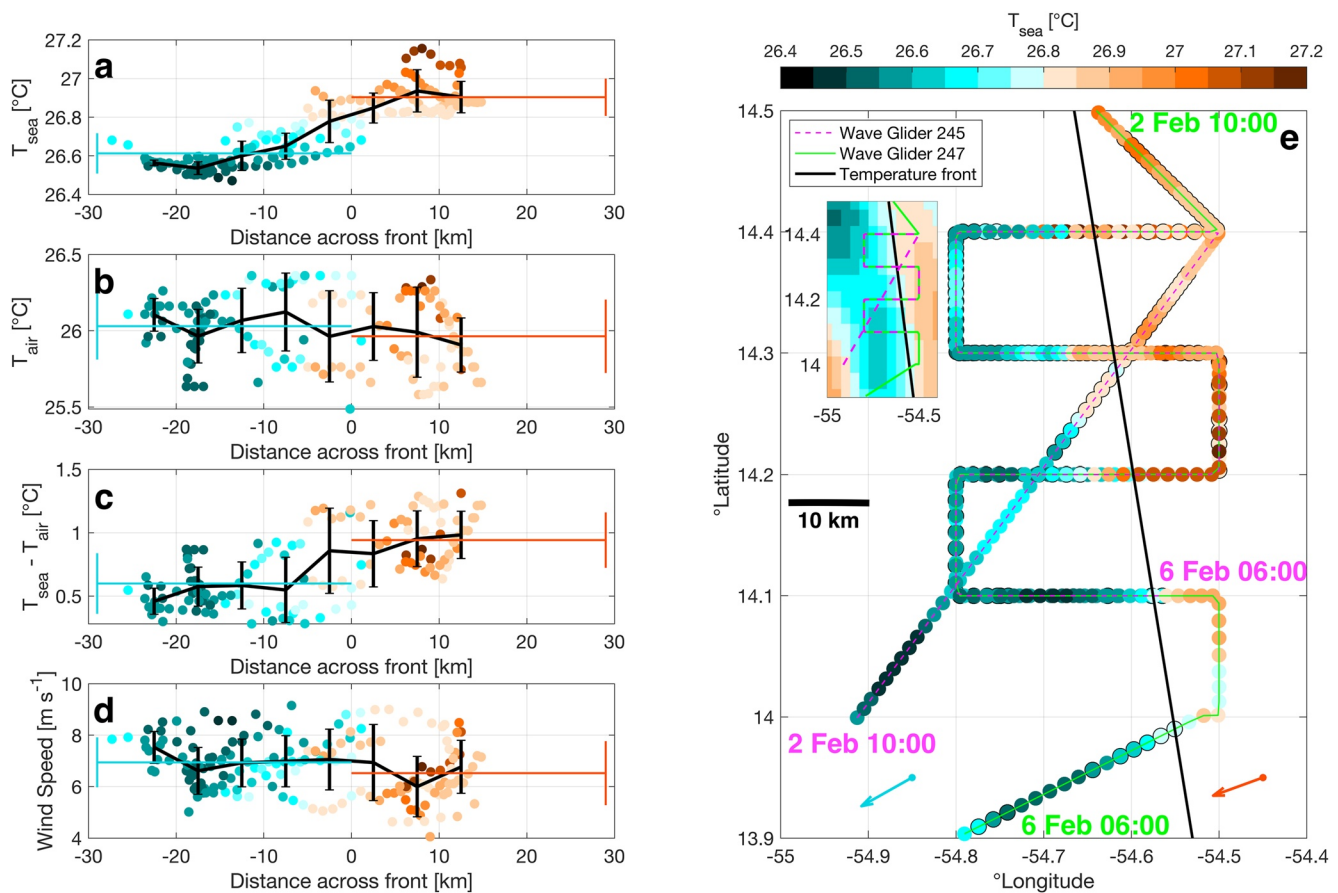
Figure 3. Distance from the sea surface temperature (SST) front versus (a) observed SST, (b) air temperature, (c) sea minus air temperature difference, and (d) wind speed from Wave Glider tracks from 2 to 6 February 2020. Colors denote SST and error bars denote averages and standard deviations within 5 km distance increments. Thin horizontal orange and blue lines represent averages and standard deviations on the warm and cold side of the SST front. (e) SST observed by Wave Glider 245 (pink track) and Wave Glider 247 (green track). The green and pink text denote the starting and ending times of the plotted tracks. Only nighttime data are shown. The SST front is shown by the black line. Orange and blue quivers denote the average wind speed and direction on the warm and cold side of the front. Inset: Front location, Wave Glider tracks, and Group for High Resolution Sea Surface Temperature (GHRSST)-Operational Sea Surface Temperature and Sea Ice Analysis (OSTIA) satellite SST observations (corrected for −0.2°C offset) from 4 February 2020.

to relative humidity, but these malfunctioned soon after deployment and their data are not shown. Analysis of air-sea fluxes from Wave Gliders will focus only on the bulk sensible heat flux. Wave Glider data shown in the present study have a temporal resolution of 30 min, with each data point representing a 20-min average sent via Iridium telemetry.

Wave Gliders are autonomous vehicles that can be remotely piloted to move at up to 2 km hr^{-1}. Wave Glider tracks were strategically programmed based on recent observations from SWIFTs, Wave Gliders, the NOAA Ship *Ronald H. Brown*, and satellites. These tracks, shown by straight lines in Figure 2a, were preferentially selected to sample significant SST gradients and systematically sample conditions that are difficult to observe with Lagrangian platforms, for instance in directions counter to the wind and/or currents. A specific benefit of using Wave Glider observations to analyze spatial variability is that Wave Gliders have the capability to cross a persistent ocean front multiple times. When a front was identified from observations, Wave Gliders were piloted to repeatedly cross it (e.g., Figure 3) and obtained high-resolution measurements of smaller-scale SST fronts. A potential complication to this strategy is that both spatial and temporal variability influence the observations; this is discussed further in Section 3.4.

3. Methods

3.1. Data Calibration and Corrections

SWIFT and Wave Glider measurements were calibrated using observations from the NOAA Ship *Ronald H. Brown* and the method described by Iyer et al. (2022). By assuming that ship and drifter observations should be identical within 5 km distance of each other (or 15 km if insufficient data were available from within 5 km), linear regressions were used to correct wind speed, relative humidity and air temperature observations (Thomson et al., 2021a). To remove the influence of diurnal artifacts, nighttime data were used for air and ocean temperature offset corrections and, for air temperature, only data collected from 22:00 to 10:00 UTC (approximately 18:00 to 06:00 local time) were used in further analysis. Root mean square uncertainties in wind speed, relative humidity and air temperature were 0.24–0.96 ms^{-1}, 0.8%–2.1%, and 0.03°C–0.58°C, respectively. Ocean temperatures were corrected by subtracting the average of each platform's value from observations from the ship's sea snake (approximately 0.05 m depth) when a platform was within 2 or 5 km of the ship. These corrections were typically <0.1°C.

3.2. Bulk Flux Calculations

Version 3.6 of the COARE bulk flux algorithm (updated from Edson et al., 2013; Fairall, Bradley, Rogers, et al., 1996; Fairall et al., 2003) was used to calculate air-sea fluxes from SWIFT and Wave Glider observations. Bulk sensible heat, latent heat, and upward buoyancy fluxes can be calculated from observed atmospheric and oceanic parameters as:

$$SHF = \rho_a C_p C_H \left(U - U_c\right) \left(T_{sea} - T_{air}\right), \tag{1}$$

$$LHF = \rho_a L_v C_E \left(U - U_c\right) \left(q_{sea} - q_{air}\right), \tag{2}$$

and

$$UBF = SHF + \left(0.61 \times LHF \times C_p \times T_{air}/L_v\right), \tag{3}$$

respectively. ρ_a is the air density, C_p is the specific heat capacity of air, L_v is the latent heat of vapourization, C_H and C_E are the transfer coefficients of sensible heat and latent heat (moisture), U—U_c is the surface current-relative wind velocity, T_{sea} is the SST, T_{air} is the air temperature, q_{sea} is the sea surface saturation specific humidity, and q_{air} is the air specific humidity. COARE 3.5 and 3.6 parameterize the air-sea transfer coefficients based on the atmospheric stability, height of the measurements, wind speed, and the wave-dependent roughness length (Edson et al., 2013; Fairall, Bradley, Rogers, et al., 1996; Fairall et al., 2003); COARE 3.6 improves on this by utilizing a wave model (Banner & Morison, 2010) to parameterize the effect of wave age on surface roughness and stress. Differences between sensible and latent heat fluxes calculated with COARE 3.6 and fluxes calculated using a prior wind speed-dependent transfer coefficient parameterization (Jaimes et al., 2015) were on average less than 10% (not shown). Thus, fluxes are insensitive to the choice of parameterizations, that is, 3.5 or 3.6. Fluxes were only calculated when all relevant atmospheric or oceanic observations were available, with two exceptions: First, when air pressure and wind speed observations were not available from SWIFTs, measurements from nearby drifters were substituted because those parameters were generally spatially invariant. Second, even though local humidity observations were not made from Wave Gliders, sensible heat fluxes are still reported as sensible heat flux is insensitive to humidity. We reiterate that calculations presented here are of bulk fluxes calculated from 10- or 20-min mean fields, not direct eddy covariance flux measurements which are not possible to calculate from this data set.

3.3. Analysis Strategy and Sensitivity Experiments

In situ SST observations were used to identify when significant SST gradients existed across Wave Glider tracks or between different SWIFT drifters. For case studies, a threshold SST was visually identified to separate areas of relatively warm and cold water. SST frontal locations were verified with satellite SST maps. In the Wave Glider cases, the orientation of fronts was defined by selecting points in space with observed temperatures within 0.02°C of this threshold and performing a linear regression of latitude versus longitude. Different techniques, including using piece-wise functions and SST gradients to define the frontal position, were also tested and produced

negligibly different results. Thus, using this method leads to minimal artificial smoothing. This procedure was not used in SWIFT cases because drifters did not typically cross fronts and thus a clear frontal boundary could not be identified. To distinguish cases where the spatial ocean structure was observed directly (Wave Gliders) from cases where gradients were inferred as the difference between two point measurements separated in space (SWIFTs), we hereinafter only use the term "front" to refer to spatial SST variations observed by Wave Gliders. Fluxes were then compared on both sides of the defined front (Wave Gliders) or between areas with temperatures above and below the SST threshold (SWIFTs). A combined analysis of all of the periods of time when significant SST gradients existed was then used to evaluate the spatial variability of fluxes across these gradients.

A goal of the present study is to evaluate the influence of individual components on air-sea fluxes with a specific emphasis on SST, the primary parameter through which ocean fronts affect air-sea interaction. Two COARE sensitivity tests were conducted for each case study to isolate the effect of spatial ocean (SST) variability from the influence of atmospheric (air humidity, temperature, wind) variations on fluxes. Thus, COARE was run a total of three times to calculate fluxes for each case:

- Observed
- "Ocean-variability-only" (OV) sensitivity tests
- "Atmosphere-variability-only" (AV) sensitivity tests

"Observed" simply refers to bulk fluxes calculated using the observed ocean and atmospheric parameters from SWIFTs or Wave Gliders as inputs (see Section 3.2). The first set of sensitivity tests, OV, involved calculating fluxes using the observed SST but constant regionally-averaged (average value from all SWIFT or Wave Glider observations during a given period of time) atmospheric parameters as inputs into COARE. That is, atmospheric parameters including air temperature, humidity, and wind speed were kept constant. These tests represent the fluxes that would be present if SST gradients exist but the atmosphere was invariant in this region and time period. Similarly, AV fluxes involved calculating fluxes with COARE using observed atmospheric parameters and regionally-averaged ocean parameters. Using spatially-averaged parameters to isolate the influence of individual or sets of variables on fluxes is analogous to the temporally-smoothed parameters used in sensitivity tests by previous studies to isolate the influence of high-frequency versus low-frequency SST (DeMott et al., 2016; Gao et al., 2019; Shinoda et al., 1998) or atmospheric variables (Dellaripa & Maloney, 2015) on surface fluxes.

3.4. Isolating Diurnal and Temporal Variability From Spatial Variability

Several techniques were used to isolate the effects of spatial variability from temporal variability (e.g., fluctuations in Figure 1 insets) in Wave Glider observations. Wave Gliders were programmed to move at near their maximum speed so that measurements can be interpreted as snapshots in time as much as possible. To minimize the influence of temporal nighttime air temperature variability, the two Wave Gliders were strategically directed to obtain simultaneous measurements of both sides of a gradient. One such technique used frequently during the second leg of ATOMIC (e.g., Figure 3) involved directing the Wave Gliders to follow the same path with a set time lag. For SWIFT drifters, observations from multiple drifters located across gradients at the same time were used to assess spatial variability.

4. Results

4.1. Background Conditions During ATOMIC

Figure 2 shows histograms of observations from SWIFTs and Wave Gliders during the entirety of the ATOMIC campaign, which were generally consistent with observations from the nearby NOAA Ship *Ronald H. Brown* (Figure 1 inset). Averaged over the ATOMIC data set, the air-sea (sea minus air) temperature and specific humidity differences were 0.86°C and 5.4 g kg^{-1}, which imply positive upward heat, moisture, and buoyancy fluxes. COARE 3.6 calculations showed that bulk air-sea sensible heat, latent heat, and upward buoyancy fluxes were on average 6.6, 157, and 16.5 Wm^{-2}, respectively. In this paper, positive flux values denote upward fluxes from the ocean to the atmosphere.
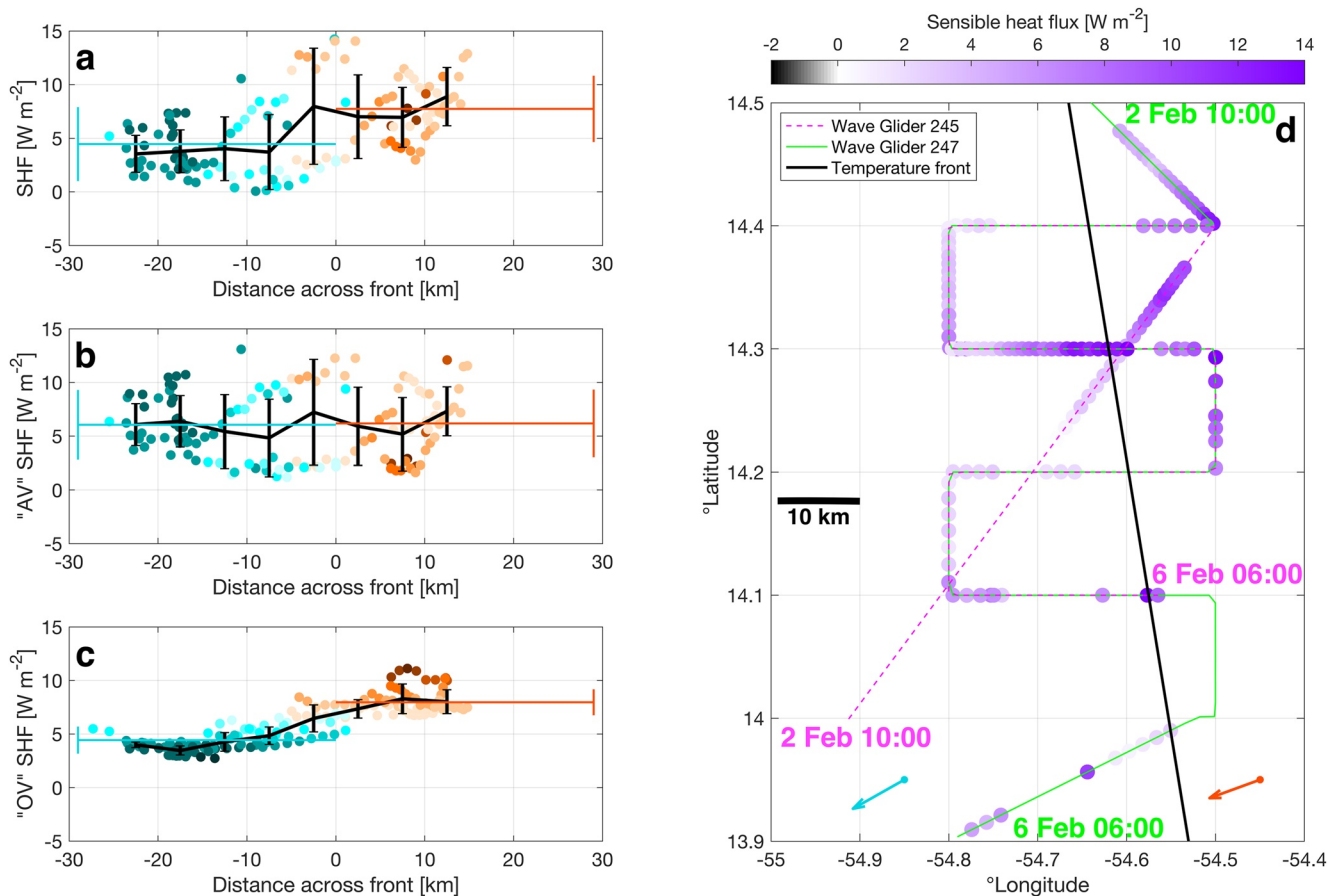
Figure 4. Distance from the sea surface temperature (SST) front versus (a) observed sensible heat flux, (b) "atmosphere variability only" (AV) sensible heat flux, and (c) "ocean variability only" (OV) sensible heat flux. As with Figures 3a–3d, colors denote SST, error bars denote averages and standard deviations within distance bins, and thin horizontal lines represent averages and standard deviations on the warm and cold side of the SST front. (d) Map of Wave Glider tracks with colors denoting nighttime observed sensible heat flux. Lines, text, and quivers denote the same parameters as in Figure 3e.

4.2. Case Studies

4.2.1. Case 1: Wave Gliders Drive Across a Persistent Front

From 2 to 6 February 2020, two Wave Gliders repeatedly crossed over a persistent SST front with approximately a 12 hr time lag (Figure 3). We define the front's position in space (Figure 3e) using linear regression of observations where the SST was near a 26.8°C threshold. The observed SST front is consistent with the SST gradient observed in GHRSST-OSTIA satellite observations (Figure 3g inset), although the satellite observations are biased cold by 0.2°C compared to Wave Glider observations. This is slightly larger but in the same direction as the average 0.08° cool skin-corrected bias in satellite SSTs reported by Wick et al. (2022) in the ATOMIC region. Wind speeds and nighttime air temperatures did not show consistent spatial trends and instead exhibited high-frequency variability. Wind directions were consistently from the northeast on both the warm (average direction of 75°) and the cold (68°) sides of the front; thus wind blew across the front from warm to cold water. That is, in contrast to the observations of Shao et al. (2019) and numerical model results (e.g., Sullivan et al., 2020), no clear spatial wind speed or directional response to SST gradients was observed. This may be a result of the small spatial scale or weak magnitude of the observed SST front.

The spatial variability of sensible heat flux estimated from COARE 3.6 (Figure 4a) mirrors that of air-sea temperature differences shown in Figure 3c, with higher values in warm water east of the front and small-scale fluctuations resulting from spatiotemporal variations in air temperature. The average sensible heat flux on the west (cold) side of the front was 4.1 Wm^{-2}, approximately 50% lower than the average sensible heat flux on the warm side (Figure 4a). This is a significant difference considering that average sensible heat fluxes were only 6.6 Wm^{-2}
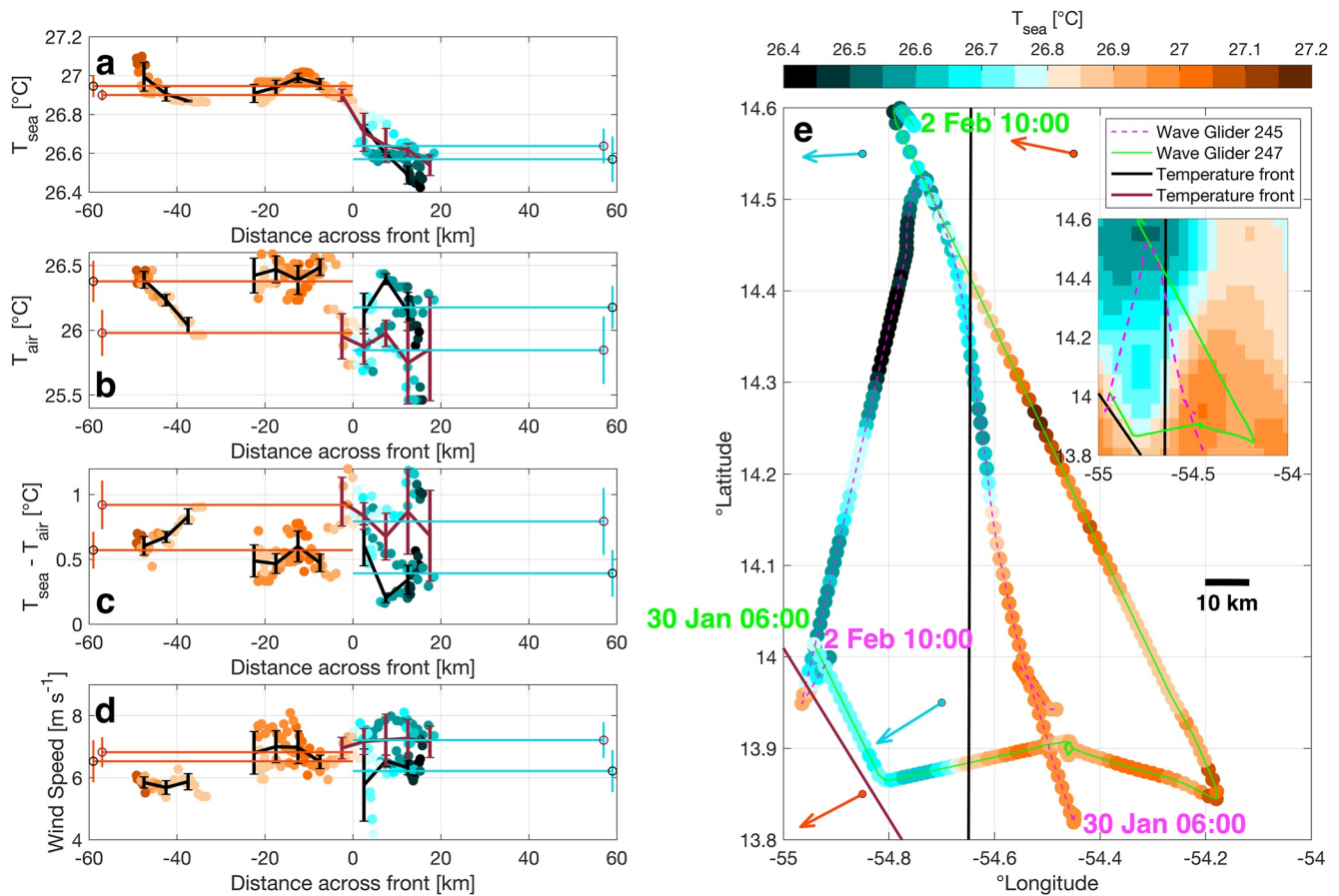
Figure 5. Same as Figure 3 for case study 2 (30 January to 2 February 2020). Group for High Resolution Sea Surface Temperature (GHRSST)-Operational Sea Surface Temperature and Sea Ice Analysis (OSTIA) satellite Sea surface temperature (SST) observations in Figure 5a are from 1 February 2020 and are offset by +0.4°C to match in situ observations. The red line denotes the position of the second (southwestern) sea surface temperature (SST) front. Orange and blue quivers in the northern and southern part of the domain denote the average wind speed and direction on the warm and cold side of the eastern (black) and southwestern (red) front, respectively. Error bars and open circles in panels (a–d) represent binned-averages, mean, and standard deviation of the front of the same color in (e).

throughout ATOMIC (Figure 2). Correlation between SST and sensible heat flux on spatial scales under 10 km was also observed by Shao et al. (2019) across larger SST gradients. Because of the formulation of the air-sea buoyancy flux (Equation 3; Johnson et al., 2001), sensible and latent heat fluxes contribute almost equally to the buoyancy flux in these tropical oceanic conditions and thus it is likely that the buoyancy flux significantly varies across the front as well. However, we cannot quantify this without collocated humidity measurements.

Results from the OV and AV sensitivity tests are shown in Figures 4b and 4c. The average slope of the OV flux (Figure 4c) resembles the average slope in the observed fluxes (Figure 4a) within 10 km of the frontal boundary, which suggests that the SST drove the linear increase in fluxes across the front. However, excluding the average linear east-west variability, the observed and AV fluxes (Figures 4a and 4b) very closely resemble each other: both exhibit similar high-frequency fluctuations at all locations in space. This implies that the atmosphere has a dominant role in modulating variations in air-sea fluxes on short temporal scales, both close to and farther away (>10 km) from the frontal boundary. The sharp sensible heat flux gradient 5 km west of the frontal boundary appears to be driven by a combination of ocean and air temperature gradients.

4.2.2. Case 2: Wave Gliders Drive Across Two Sharp SST Fronts

Two sharp SST fronts were observed from 30 January 2020 to 2 February 2020. Satellite SST was biased cold by 0.4°C, with fronts slightly offset in position relative to Wave Glider SST. SST varied throughout the domain by 0.7°C (Figure 5a) but was mostly constant on both sides of the frontal boundaries. Air temperatures were considerably warmer on average (0.2°C) on the warm ocean sides of both fronts. Thus, SST and air tempera-
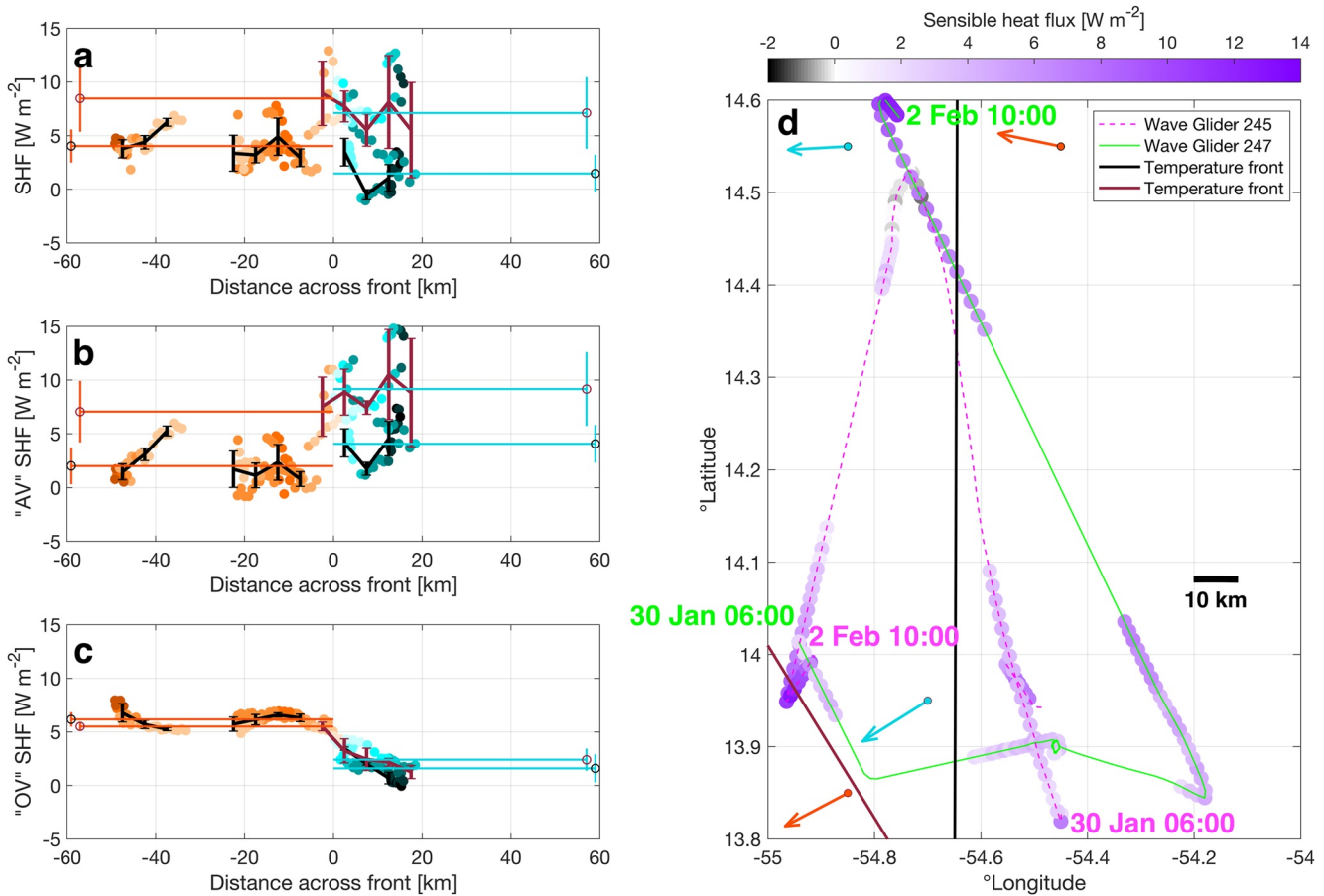
Figure 6. Same as Figure 4 for case study 2 (30 January to 2 February 2020). The red line denotes the position of the second (southwestern) sea surface temperature (SST) front. Error bars and open circles in panels (a–c) represent binned-averages, mean, and standard deviation of the front of the same color in (d).

ture tendencies partially cancel out, so air-sea temperature differences are moderate compared to case study 1 (Figure 5c). Wind speeds and directions were similar on both sides of both fronts and did not show clear evidence of a wind response to the observed SST fronts.

Average sensible heat flux was 8.5 Wm^{-2} on the warm side and 7.1 Wm^{-2} on the cold side of the southwestern SST front. These values were 4.0 and 1.7 Wm^{-2}, respectively, across the eastern front (Figure 6). Fluxes were higher and more spatially variable near the southwestern front because of colder and more variable air temperatures over this region (Figure 5b). In contrast to case 1, OV and AV sensible heat fluxes are elevated on opposite sides of the ocean fronts: mean OV fluxes are higher by 3.1 Wm^{-2} (southwestern front) and 4.6 Wm^{-2} (eastern front) on the warm sides of the fronts. However, mean AV fluxes are lower by 2.1 Wm^{-2} (both fronts) on the warm ocean sides of the fronts (Figures 6b and 6c). These values suggest that SST gradients drive the spatial variability of the sensible heat flux, but that the atmosphere partially cancels out the influence of SST gradients on the average sensible heat flux across the front. While average sensible heat flux differences were small, strong spatial gradients were observed across both fronts during the night of 1–2 February consisting of abrupt sensible heat flux changes of 4 Wm^{-2} across less than 10 km (Figures 5a, 5b, and 5d inset). OV data also show a strong flux gradient (3–3.5 Wm^{-2}) across frontal boundaries, but AV fluxes only show weak gradients ($\leq$2 Wm^{-2}). These findings suggest that, in the vicinity of frontal boundaries, SST gradients are largely responsible for sensible heat flux gradients. However, as shown by the similarities between the observed and AV fluxes and consistent with case 1, atmospheric variability (spatial and/or temporal variations in air temperature from atmospheric boundary layer turbulence, cold pools, or convective structures) dominates high-frequency air-sea flux variations farther away from the boundaries. A possible cause of these patterns may be that the atmosphere partially equilibrates to SST gradients. That is, further away from the SST front where water is warm (or cold), the atmosphere may
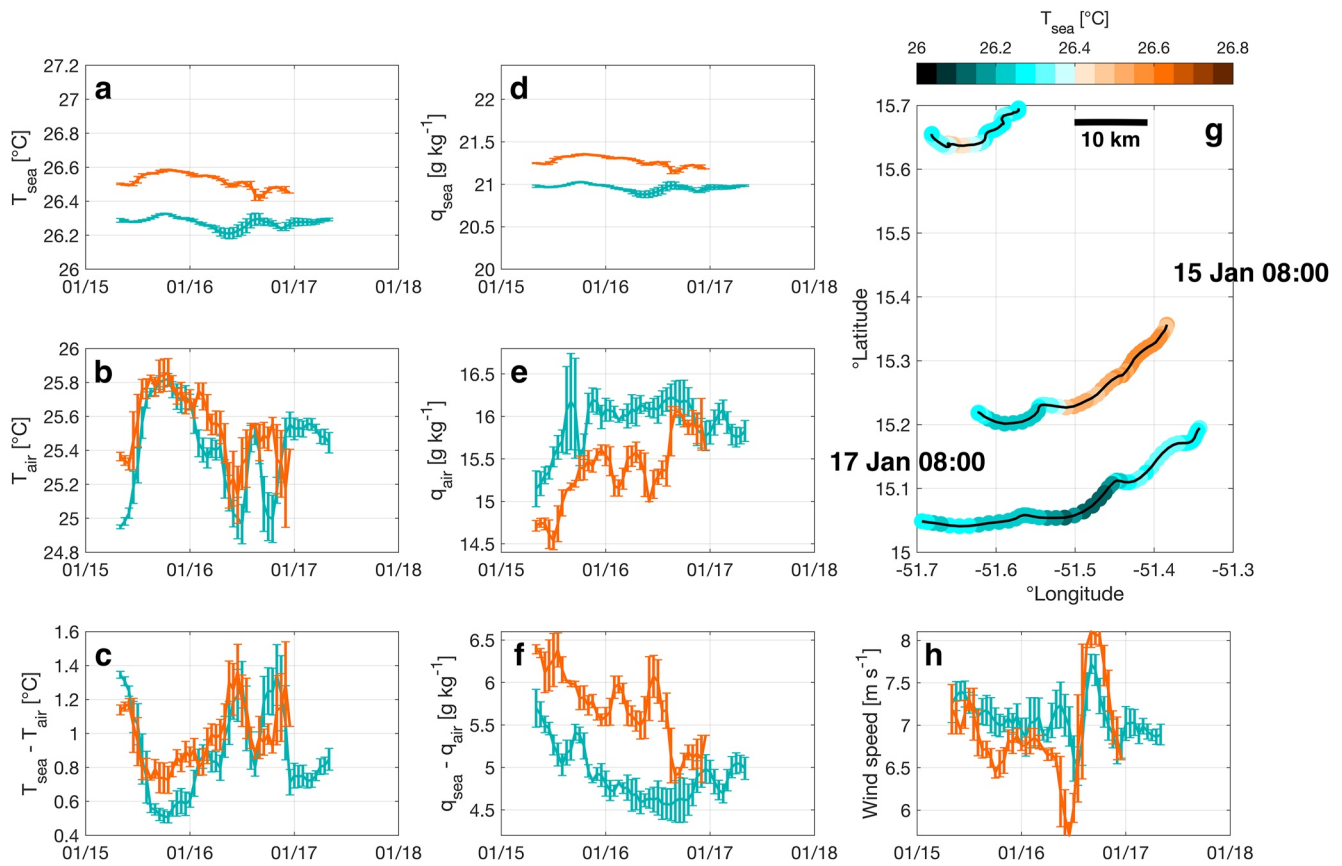
Figure 7. Time series of hourly average and standard deviation (error bars) of (a) sea surface temperature (SST), (b) 0.5 m air temperature, (c) sea minus air temperature, (d) ocean surface saturation specific humidity, (e) 0.5 m air specific humidity, (f) ocean minus air specific humidity, and (h) wind speed corrected to 10 m in areas with warm water (SST > 26.4°C; orange) and cold water (SST < 26.4°C; blue) observed by Surface Wave Instrument Float with Trackings (SWIFTs) from 15 to 17 January 2020. (g) Map of SST observed by SWIFTs.

have had ample time or opportunity to warm in response to warmer water (or, cool in response to colder water). However, near (within 10 km of) the front, the atmosphere does not consistently respond to SST gradients on either side, leading to the stronger spatial gradients shown in Figure 6a.

4.2.3. Case 3: SWIFTs Drifting Across a Temperature Gradient

Near the start of leg 1 of ATOMIC, the SWIFTs were strategically deployed across an SST gradient and then drifted southwestward from 15 January 2020 08:00 UTC to 17 January 2020 08:00 UTC. We note that this is the same period of time as case 2 in Iyer et al. (2022). Satellite SST data (see Section 5.1) confirm that the orientation of the gradient varied in space: a warm tongue of water (defined as SST > 26.4°C) extended eastward from the west and encompassed the central area of the domain (Figure 7g). Air temperatures and wind speeds were usually similar (within 0.1°C and 0.5 ms^{-1}) whether water was warm or cold (Figure 7b), while average specific humidity was 0.5 g kg^{-1} greater over cold water (Figure 7e). Wind directions in the area were consistently from the northeast.

COARE 3.6 simulations and sensitivity tests were used to compute heat fluxes and analyze spatial flux variations. Because humidity data are available from SWIFTs, bulk latent heat and buoyancy fluxes were also calculated. Latent heat fluxes were on average 25 Wm^{-2} (14%) greater over warm water than cool water (Figures 8a, 8d, and 8g) owing to large differences in air specific humidity (Figures 7e and 7f). However, sensible heat flux differences (0.6 Wm^{-2}; 6%) and upward buoyancy flux differences (2.4 Wm^{-2}; 10%) across the SST gradient were small. AV and OV sensitivity tests (Figure 8) suggest that spatial flux variations (i.e., differences between the orange and blue lines in Figures 8a, 8d, and 8g) are driven jointly by the atmosphere and ocean. For sensible heat flux, warmer air temperatures on the warm ocean side partially cancel out the ocean's influence on air-sea
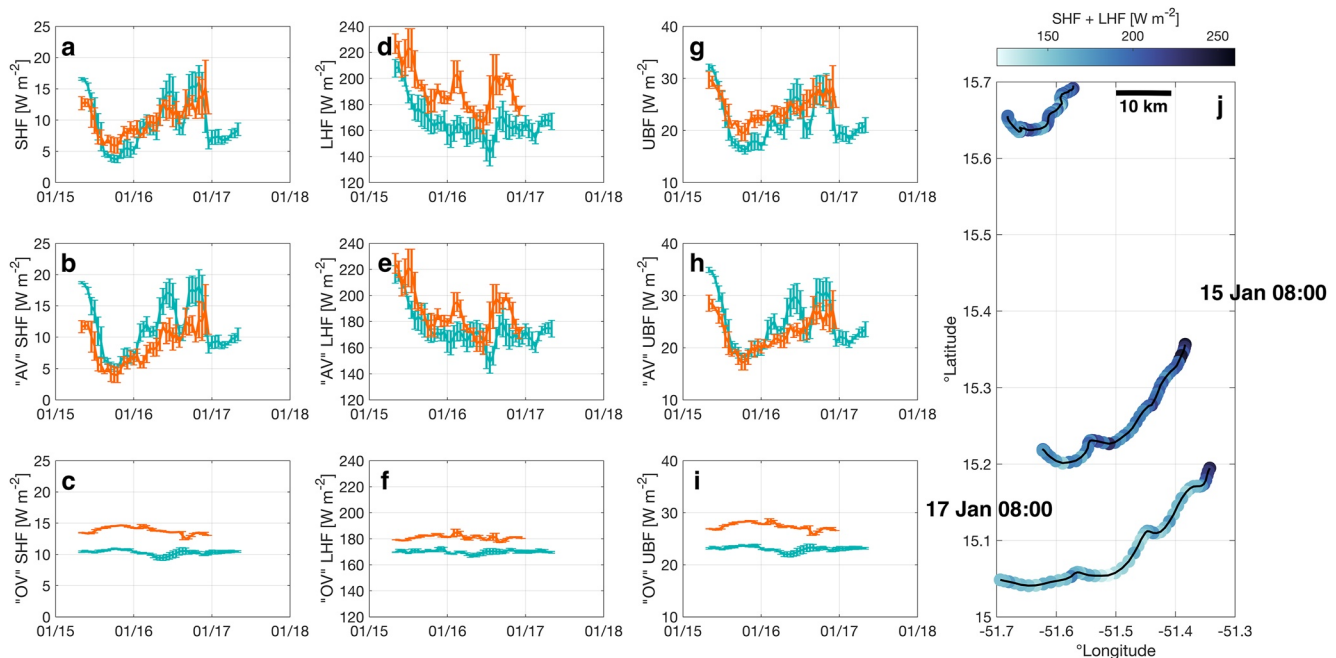
Figure 8. Time series of hourly average and standard deviation (error bars) of (a) sensible heat flux, (b) "atmosphere-variability-only" (AV) sensible heat flux, (c) "ocean-variability-only" (OV) sensible heat flux, (d) latent heat flux, (e) AV latent heat flux, (f) OV latent heat flux, (g) upward buoyancy flux, (h) AV upward buoyancy flux, and (i) OV upward buoyancy flux in areas with warm water (sea surface temperature [SST] > 26.4°C; orange) and cold water (SST < 26.4°C; blue) observed by Surface Wave Instrument Float with Trackings (SWIFTs) from 15 to 17 January 2020. (j) Map of sensible plus latent heat flux observed by SWIFTs.

temperature difference. For latent heat flux, higher SST (i.e., higher sea surface specific humidity) and lower air specific humidity on the warm ocean side led to the greater latent heat flux there.

While SST gradients played a significant role in modulating spatial flux differences, atmospheric changes were responsible for the strongest magnitude temporal variations in air-sea fluxes. Because air temperature, wind speed, and humidity vary at a faster rate and by larger amounts than SST (e.g., Figures 7b vs. 7a), atmospheric variability dominates and can be seen as distinct similarities in the time series of observed and AV fluxes (i.e., Figures 8a, 8d, and 8g are similar to Figures 8b, 8e, and 8h). For example, around midday on 15 January, air temperature and specific humidity increased faster on the cold ocean side than the warm side (Figures 7b and 7e), leading to enhanced flux gradients across the SST front. We hypothesize that strong atmospheric variations on timescales of hours are due to turbulent overturning eddies, small-scale convective motions, or wind surges influencing dry air entrainment across the boundary layer top. Temporal air temperature, wind speed, and specific humidity variations also occur on 16 January and influence air-sea fluxes: a decrease in air temperature from 25.6°C to 25°C and increase in wind speed from 6 to 8 ms^{-2} was observed over warm and cold water, leading to an increase in sensible heat and upward buoyancy flux of over 5 Wm^{-2} and an increase in latent heat flux of around 30 Wm^{-2} for several hours. This highlights the role that wind speed plays in modulating air-sea fluxes: even though wind speeds are spatially invariant, temporal variability can drive air-sea flux variability. The atmospheric variations are likely the result of an atmospheric cold pool: similar sudden drops in air temperature were observed by the NOAA Ship *Ronald H. Brown*, which was around 60 km away from the drifters (not shown).

4.3. Synthesis of All Data

4.3.1. Spatial Gradients in the ATOMIC Region

Figure 1 and the case studies demonstrate that SST gradients were frequently observed during ATOMIC. This section presents a statistical analysis of gradients. Spatial differences across a given field are denoted by Δ and are assessed by calculating differences between two SWIFT drifters at any given point in time. SST differences between any two drifters (ΔT_{sea}) varied between 0.01°C and 0.73°C, with an average of 0.35°C and a standard deviation of 0.19°C. $\Delta T_{sea} > 0.3$°C for a total of 243 hr (52% of the total deployment time), and $\Delta T_{sea} > 0.5$°C for

140 hr (30% of the total time). The average sharpness of fronts was also highly variable: SST gradients between drifters were between 0.001°C and 0.047°C km^{-1} with an average of 0.008°C km^{-1} and a standard deviation of 0.005°C km^{-1}. Particularly sharp gradients of over 0.01°C km^{-1} were observed for 77 hr (16% of the total deployment time). These SST gradients occurred across distances of 10–100 km, consistent with submesoscale to mesoscale ocean features. SST gradients persisted for as long as several days (e.g., Figures 3, 5, and 7).

Throughout ATOMIC, considering only drifter-pairs with $\Delta T_{sea} > 0.3°C$, air temperatures were, on average, 0.10°C higher over warmer water. In total, 62% of the SWIFTs on warm sides of strong SST gradients also measured warmer air temperature. Air specific humidity was also usually (65% of the time) higher on the warm side of strong gradients; the average difference was 0.14 g kg^{-1}. Wind speed differences were 0.4 ms^{-1} lower on average on the warm side of strong gradients, but were highly variable in both space and time and thus not consistently significantly lower on the warm side of gradients.

4.3.2. COARE Sensitivity Tests

Using the average relationships between observed variables presented above, we now test the sensitivity of COARE 3.6 for the hypothetical flux gradient caused by a given SST gradient. Assuming that spatial air temperature and specific humidity variations are present across a strong 0.51°C ocean gradient (the average of observed ΔT_{sea} when $\Delta T_{sea} > 0.3°C$) and are equal to the average values stated in the previous subsection, the sensible heat flux, latent heat flux, and upward buoyancy flux will vary across the gradient by 6.9 Wm^{-2} (76%), 20.9 Wm^{-2} (10%), and 8.5 Wm^{-2} (34%), respectively. These variations indicate that significant spatial flux gradients relative to mean values, especially for sensible heat flux, will typically occur across 10–100 km SST gradients in the tropical Atlantic trade wind region.

To assess the magnitude of typical flux gradients in the ATOMIC region (as opposed to the strong SST gradients described in the previous paragraph), we perform the same sensitivity tests using a 0.35°C SST gradient, the average difference observed between pairs of SWIFTs during ATOMIC. Incorporating average atmospheric gradients, the resulting sensible heat flux, latent heat flux, and upward buoyancy flux will increase on the warm side of the SST gradient by 5.6 Wm^{-2} (62%), 18.8 Wm^{-2} (9%), and 7.0 Wm^{-2} (28%), respectively. These flux gradients are weaker than the gradients expected when ΔT_{sea} is large, but still demonstrate that non-negligible variability would be expected in the ATOMIC region, even in the absence of a strong SST gradient. As seen in the case studies, significant variations in surface fluxes are driven by SST gradients, even as atmospheric adjustments tend to homogenize or eliminate those flux gradients.

4.3.3. Flux Variations Across Persistent SST Gradients

While the sensitivity analysis provides insight into the how fluxes varied across SST gradients on average, it does not address the fact that SST gradients were associated with differing spatial atmospheric patterns or that SST gradients were observed across a wide range of distances. To address these points, we identify three persistent SST gradients (Figure 9) and perform a targeted analysis of the influence of individual parameters on air-sea fluxes from SWIFT drifters on either side of gradients. The SST gradients shown here, which include the three case studies in Section 4.2, collectively span 17 total days of observations and over 80% of the time during which SWIFTs were deployed. The spatial consistency between observations and daily satellite data suggests that these SST gradients are large-scale persistent features which are not associated with temporal variability. Further supporting this evidence of submesoscale to mesoscale ocean variability is the observation that drift tracks observed across SST gradients 2 and 3 indicate that surface currents on either side of the SST gradient were different, with more variable currents on the cold ocean side (Figures 9b and 9c). The differences (warm ocean side minus cold ocean side) in distance (spacing between drifters), fluxes of sensible heat, latent heat, and upward buoyancy (SHF, LHF, UBF), and their components of air specific humidity and temperature and air-sea differences of those quantities (q_{air}, T_{air}, $T_{sea} - T_{air}$, and $q_{sea} - q_{air}$) are shown in Figures 10 and 11. Figure 10 also shows the expected influence of these variations on sensible and latent heat flux as background contours. Figure 11 shows the correlation between gradients of sensible heat, latent heat, and upward buoyancy flux, as well as gradients of their components, with colors representing the distance between drifters.

First, it is important to note that the three large-scale SST gradients occupy different regions of the flux parameter space shown in Figures 10 and 11 and thus gradients are not generalizable in a composite sense: Gradient 3 (3–10 February; diamonds on Figures 10 and 11) was associated with high ΔT_{sea} and Δq_{air} (Figures 10a and 10d) and low ΔT_{air} (Figure 10a), while gradient 1 (14–18 January; circles on Figures 10 and 11) was associated with
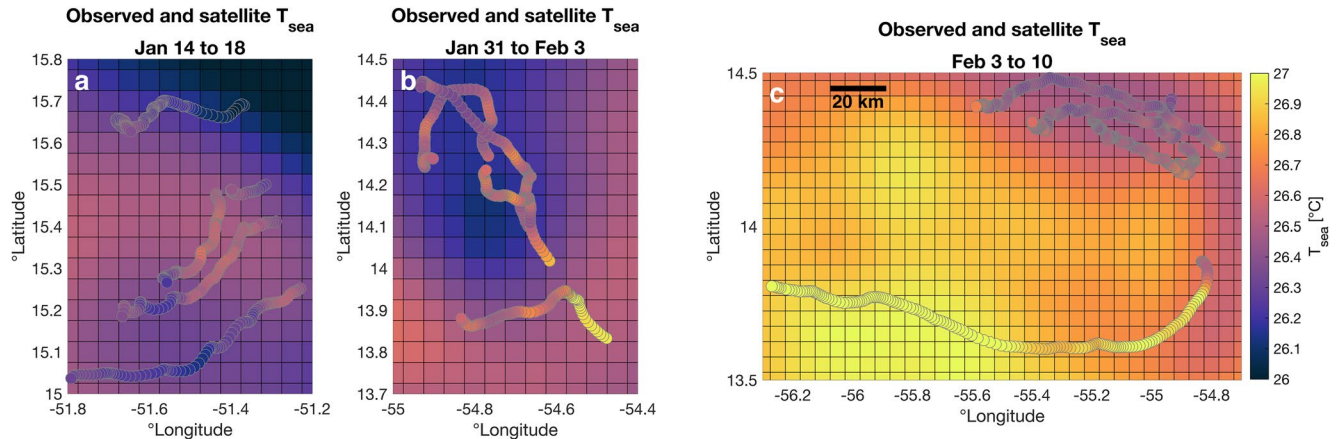
Figure 9. Observed sea surface temperature (SST) plotted on a background of Group for High Resolution Sea Surface Temperature (GHRSST)-Operational Sea Surface Temperature and Sea Ice Analysis (OSTIA) satellite SST taken midway through each a time period during which a persistent SST gradient was observed on (a) 14–18 January 2020, (b) 31 January to 3 February 2020, and (c) 3–10 February 2020.

moderate ΔT_{sea}, negative Δq_{air}, and high ΔT_{air} (Figure 10a) across the SST front (Figure 10d). Gradient 2 (31 January to 3 February; squares on Figures 10 and 11) exhibited a mix of characteristics from gradients 1 and 3.

Although atmospheric and oceanic parameters vary on a case-by-case basis, Figure 10 still provides quantitative insight into the influence that individual parameters, including SST and atmospheric variables, are expected
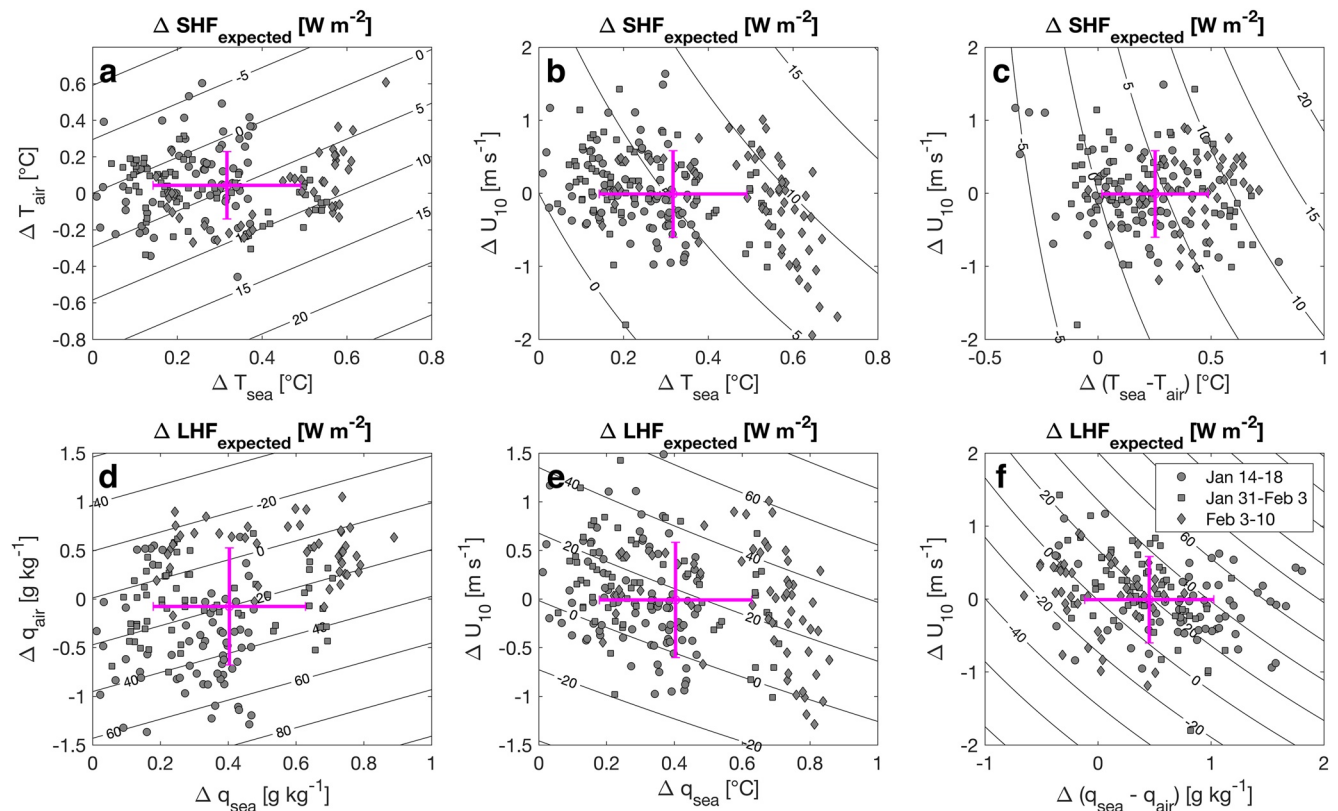

Figure 10. Change in ocean parameters, atmospheric parameters, and air-sea differences across three persistent gradients during Atlantic Tradewind Ocean-atmosphere Mesoscale Interaction Campaign (ATOMIC). Contour lines show expected change in (a–c) sensible heat flux or (d–f) latent heat flux based on values on the *x*- and *y*-axes assuming average conditions observed during ATOMIC. Marker shapes indicate gradient number (circle: gradient 1, 14–18 January; square: gradient 2, 31 January to 3 February; diamond: gradient 3, 3–10 February). Pink error bars denote mean and standard deviations of changes across all of the three time periods.
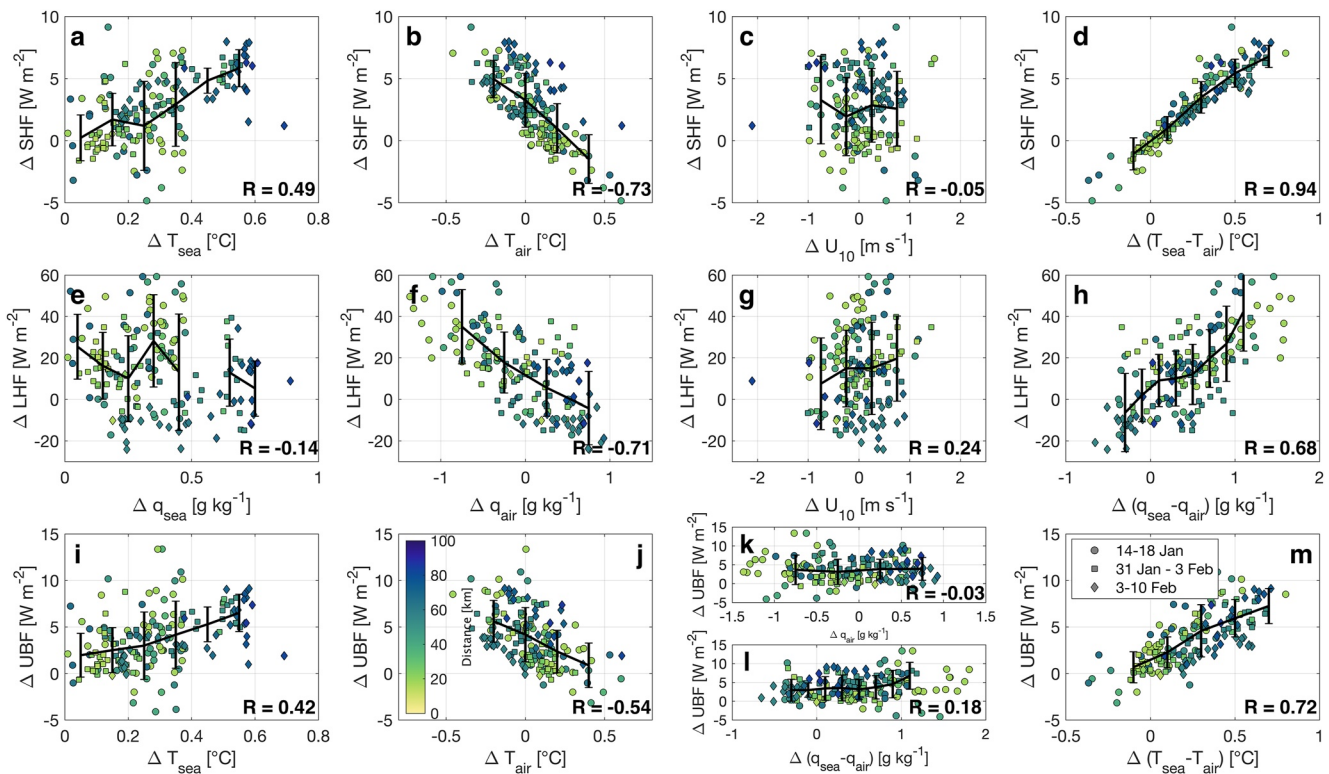
Figure 11. Change in (a, i) sea surface temperature (SST), (e) sea surface saturation specific humidity, (b, h) air temperature, (f, k) air specific humidity, (c, g) wind speed, (d, m) air-sea temperature difference, or (h, l) air-sea humidity difference versus change in air-sea (a–d) sensible heat, (e–h) latent heat, and (i–m) upward buoyancy flux across three persistent gradients during Atlantic Tradewind Ocean-atmosphere Mesoscale Interaction Campaign (ATOMIC). Marker colors denote distance between plotted observations and marker shapes indicate gradient number (circle: gradient 1, 14–18 January; square: gradient 2, 31 January to 3 February; diamond: gradient 3, 3–10 February). Black error bars denote average and standard deviations of observations within data binned by the property denoted on the *x*-axis. "*R*" values shown on the bottom right of represent linear correlation coefficients of property (*x*-axis) versus flux (*y*-axis) for each panel.

to have on gradients of air-sea fluxes in the Atlantic trade wind region during the boreal winter. SST gradients would be expected to drive sensible heat flux gradients of up to 5–10 Wm^{-2} (horizontal spread across contours in Figures 10a and 10b) and latent heat flux gradients (as sea surface specific humidity and SST are directly proportional) of up to 20 Wm^{-2} (horizontal spread across contours in Figures 10d and 10e). The vertical spread across contours in Figure 10 shows that air temperature, wind speed, and air humidity would be expected to result in sensible and latent heat flux gradients of up to 10 and 50 Wm^{-2}, respectively. The combined contribution of SST and atmospheric variables (including the air-sea differences) would thus be expected to result in sensible and latent heat flux gradients of over 10 and 50 Wm^{-2} (diagonal spread across contours in Figures 10c and 10f); that is, greater variability than from SST gradients alone.

Aggregating data from the three fronts, the observed spatial gradients of sensible heat, latent heat, and upward buoyancy fluxes were as high as 10, 50, and 10 Wm^{-2}, respectively (Figure 11). Average fluxes were 2.5, 15.6, and 3.7 Wm^{-2} higher, respectively, on the warm ocean side of gradients. The strong correlation between ΔT_{sea} and ΔT_{air} and ΔSHF (Figures 11a and 11b) and even stronger correlation between $\Delta(T_{\text{sea}} - T_{\text{air}})$ and ΔSHF (Figure 11d) suggests that gradients in SST and air temperature modulate gradients in sensible heat flux, with a negligible contribution from wind speed (Figure 11c). Quantitatively, comparing the typical highest and lowest ΔSHF values across the range of observed ΔT_{sea} and ΔT_{air} (i.e., binned averages in Figures 11a and 11b), the SST and T_{air} contributions are individually up to approximately 5 Wm^{-2}.

ΔLHF, on the other hand, is highly variable across SST fronts, uncorrelated with Δq_{sea} (and therefore ΔT_{sea}; Figure 11e), strongly correlated with Δq_{air} (Figure 11f), and moderately correlated with ΔU_{10} (Figure 11g). This suggests that latent heat flux is strongly influenced by atmospheric gradients rather than SST gradients. Furthermore, the correlation between $\Delta(q_{\text{sea}} - q_{\text{air}})$ and ΔLHF (Figure 11h) is not any stronger than the correlation between Δq_{air} and ΔLHF (Figure 11f). Comparing the highest and lowest binned average ΔLHF values, spatial

variations in q_{air} and U_{10} contribute up to 40 and 10 Wm^{-2}, respectively, to the latent heat flux. This contrasts from the expected flux contribution from SST in Figure 10 and the spread in OV sensitivity test fluxes in Figure 8: while Figure 10 indicates that SST has at least a small influence on latent heat flux gradients and is likely responsible for the positive average ΔLHF during ATOMIC, atmospheric humidity variations are much larger than SST variations and thus the atmosphere is the dominant driver of latent heat flux gradients in the region at this time of year. These atmospheric gradients may result from several processes including turbulent overturning eddies, cold pools (de Szoeke et al., 2017; Zuidema et al., 2012), or small-scale tropical convective activity (Yokoi et al., 2014). While some of the observed spatial flux gradients can persist over timescales of hours, we note that atmospheric-driven gradients generally only last for tens of minutes because atmospheric motion quickly moves coherent structures in the lower atmosphere across SST gradients and out of the domain.

Upward buoyancy fluxes are influenced by both sensible and latent heat fluxes and thus are driven by SST gradients to a lesser degree than sensible heat flux gradients but to a greater degree than that of latent heat flux gradients, as shown by the strength of correlation in Figures 11a, 11e, and 11i. Despite the strong influence of specific humidity gradients on latent heat flux gradients, the influence of specific humidity gradients on buoyancy flux gradients is near zero (Figures 11k and 11l), likely masked by the strong influence of gradients in SST and T_{air} on ΔSHF (Figure 11m). Wind speed gradients have little effect on ΔUBF ($R = 0.07$, not shown).

4.3.4. Spatial Scales of SST Gradients

Overall, as would be intuitively expected, large ΔT_{sea}, ΔSHF, and ΔUBF primarily occur when drifters are spaced farther apart (i.e., blue points on Figure 11 are associated with larger values). While this may suggest that stronger SST and flux gradients typically occur across larger distances, the presented spatial scales of variability are not comprehensively defined because SWIFTs observe individual points in space and do not resolve spatial variability between those points. For instance, SST differences between platforms tens of kilometers apart may be associated with a sharp smaller-scale front, such as the fronts observed with case study 2 (Figures 5 and 6). Regardless, it is clear that the largest differences are not observed when drifters are close together: SST gradients >0.5°C were rarely observed when drifters were closer than 50 km apart.

ΔLHF (Figures 11e–11h) was uncorrelated with the spacing between drifters. This implies that air humidity gradients, the dominant driver of spatial latent heat flux variability, often completely reversed the influence of higher q_{sea} (warmer SST) on increasing fluxes. Furthermore, this suggests that variations in air temperature, specific humidity, and wind speed, likely due to turbulent fluctuations in the atmosphere or small-scale atmospheric systems, were not consistently larger or smaller throughout the area at all scales <100 km.

5. Discussion and Conclusions

Significant submesoscale spatial SST variability was present during ATOMIC despite this being a rather quiescent area of the open ocean away from strong mesoscale eddy activity in the boreal winter. This variability may be an eventual result of the cascade of North Brazil Current eddy kinetic energy to smaller scales. The presented case studies illustrate that gradual SST gradients with changes of up to 0.7°C over tens of kilometers (e.g., Figure 3) were observed in addition to sharp fronts with SST changes of up to 0.4°C over scales less than 10 km. In all cases, air-sea sensible heat and buoyancy fluxes were consistently elevated on warm sides of SST fronts. Figure 11 quantifies spatial variability in heat, moisture, and buoyancy fluxes across scales of 10–100 km. Sensible heat fluxes and upward buoyancy fluxes varied by up to 10 Wm^{-2} between drifters spaced 10–100 km apart, while latent heat flux differences between drifters were as high as 50 Wm^{-2}. The average flux differences across these spatial scales (mean distance of 44 km) were 2.5 Wm^{-2} (sensible heat), 15.6 Wm^{-2} (latent heat), and 3.7 Wm^{-2} (upward buoyancy). Average sensible heat, latent heat, and upward buoyancy fluxes observed in the ATOMIC region were approximately 5, 157, and 16 Wm^{-2}, respectively. So, the observed differences across 10–100 km correspond to a maximum variation of roughly 200%, 30%, and 60%, respectively, of observed fluxes during ATOMIC. Average flux variations across 10–100 km were roughly 50%, 10%, and 25%, respectively. Larger proportional changes of sensible heat flux across SST gradients, compared to latent heat flux, have previously been observed in an area of stronger SST gradients (Shao et al., 2019). SST gradients drive a significant portion of the spatial variability of sensible heat flux, up to 5 Wm^{-2} (Figure 11). Air temperature variations also significantly contribute to sensible heat flux. The effect of SST on latent heat flux variability is masked by the strong impact of humidity variations (Figure 11). Wind speed variability only has a small influence on spatial
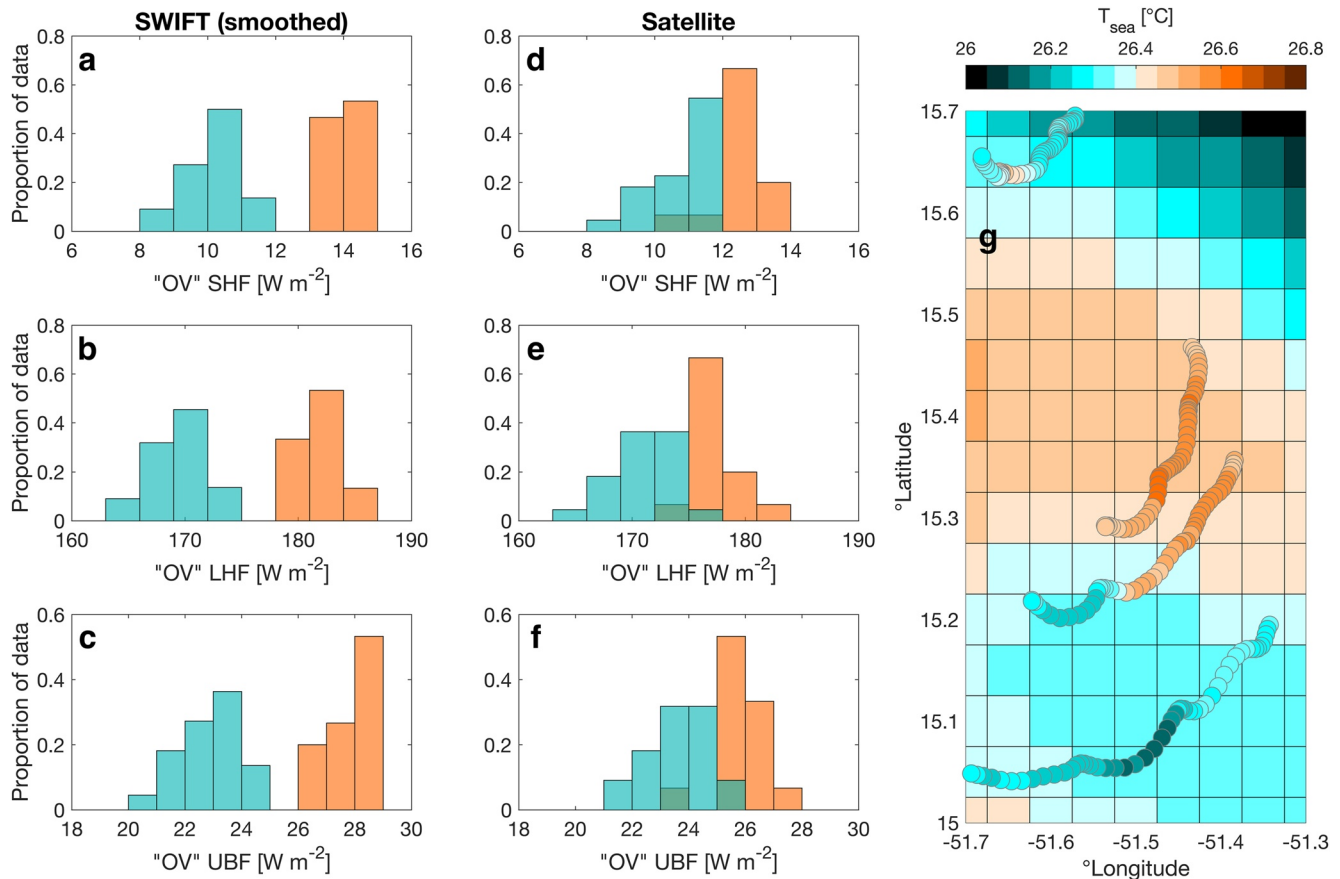
Figure 12. Histograms of "ocean variability only" (OV) (a) sensible heat flux, (b) latent heat flux, and (c) upward buoyancy flux in areas with warm sea surface temperature (SST) (>26.4°C; orange bars) and cold SST (<26.4°C; blue bars) observed by Surface Wave Instrument Float with Tracking (SWIFTs) from 15 to 17 January 2020. (d–f) are the same as (a–c), except using interpolated Group for High Resolution Sea Surface Temperature (GHRSST) Operational Sea Surface Temperature and Sea Ice Analysis (OSTIA) Level 4 satellite SST instead of SWIFT observations as inputs into COARE to calculate fluxes. (g) Map of observed SWIFT SST (15–17 January 2020) and GHRSST OSTIA Level 4 satellite SST (16 January 2020).

latent heat flux variability, and a negligible influence on variations of sensible heat or upward buoyancy fluxes across space. Unlike SST gradients, atmospheric gradients in temperature, humidity, and wind speed exist on relatively shorter spatiotemporal scales and result from a combination of turbulent fluctuations as well as atmospheric convective systems. These findings are significant because the spatial scales of variability observed here (10–100 km) are small compared to most global models and some satellite products. Lower resolution models and satellite products would not resolve the observed spatial variability in SST, air temperature, air humidity, and therefore fluxes in the tropical Atlantic trade wind region due to small spatial scale (i.e., sub-footprint-scale or sub-grid-scale) gradients.

5.1. Comparisons With a Composite Satellite Product

To gain insight into the potential uncertainty or error associated with lower resolution products in the presence of small-scale SST, atmospheric, and flux gradients, we compare bulk fluxes estimated from the SWIFT observations and fluxes estimated using SST observations from GHRSST-OSTIA, which are consistent with observed SST during ATOMIC on the satellite grid scale with only a small varying bias <0.2°C (Wick et al., 2022). Figures 12a–12c show OV fluxes from SWIFT observations smoothed to the spatial footprint of the satellite data from 15 January 08:00 UTC to 17 January 08:00 UTC, the same time period as in Figure 8. Figures 12d–12f show OV fluxes calculated using COARE 3.6 with regionally-averaged SWIFT atmospheric observations and satellite SST observed on 15–17 January as inputs. Figure 12g compares SST from the (spatially-smoothed) SWIFTs and the satellite product.

The SWIFT and satellite SST both show evidence of a central warm tongue with areas of relatively colder water to the north and south. However, comparisons of the histogram plots demonstrate that the SWIFT observations were associated with significantly stronger SST gradients and flux differences. Sensible heat fluxes estimated from the smoothed SWIFT observations differed, on average, by 3.8 Wm^{-2} between relatively warm (SST > 26.4°C) and cold (SST < 26.4°C) water. This difference was only 1.8 Wm^{-2} when estimated from satellite SST (Figures 12a and 12d). Similarly, latent heat fluxes and upward buoyancy fluxes differed, on average, by 12.3 and 4.8 Wm^{-2} in the smoothed SWIFT observations but only 5.8 and 2.2 Wm^{-2} when using satellite SST (Figures 12b, 12c, 12e, and 12f). Because the SST gradient was persistent for a longer period of time (2 days) than the temporal resolution of the satellite observations (daily), this discrepancy is likely because the satellite spatial resolution is too coarse rather than unresolved temporal variability. Quantitatively, satellite SST observations underestimate spatial flux differences across the SST front by over 50% compared to the smoothed SWIFT observations. Average fluxes throughout the entire domain were very similar for both cases and thus satellite SST observations are likely sufficient for analyzing larger-scale (>50 km) variations in this region.

Comparisons between SWIFT observations from case study 3 and the widely-used 1° by 1° OAFlux (Yu, 2019; Yu & Weller, 2007) sensible and latent heat fluxes from 16 January also yielded similar results: approximately 70% of the observed spatial sensible plus latent heat flux variability was not resolved by OAFlux estimates (not shown). This analysis suggests that when submesoscale SST gradients are not resolved in these tropical trade wind conditions, the spatial variations of air-sea fluxes across those scales will also be underestimated.

5.2. Summary

SST variability as high as 0.7°C across scales of 10–100 km was commonly observed at the ATOMIC study site in the boreal winter trade wind conditions of the northwestern tropical Atlantic, despite the fact that this region is not associated with strong mesoscale ocean activity. SST gradients were associated with air-sea flux variability of up to tens of Wm^{-2} on the same spatial scales. Across SST gradients, sensible heat fluxes varied by up to 200% (10 Wm^{-2}), while latent heat and upward buoyancy fluxes varied by up to 30% (50 Wm^{-2}) and 60% (10 Wm^{-2}), respectively. Sensible heat and upward buoyancy flux gradients vary primarily depending on the strength and relative sign of the gradients in SST and air temperature. The case study analysis demonstrates that SST gradients were sometimes the primary contributor to systematic spatial gradients in air-sea sensible heat fluxes. In other words, SST gradients were often strong enough and persistent enough to sustain spatial sensible heat flux gradients despite atmospheric effects to eliminate these gradients. On the other hand, air humidity variability was a much stronger driver of latent heat flux gradients than SST; that is, the influence of humidity variability often counteracted and sometimes reversed the influence of SST (q_{sea}) on latent heat flux. Spatial variations in wind speed were not strongly correlated with spatial variations in fluxes during this field campaign.

Comparisons between a satellite SST product and in situ observations smoothed to the satellite footprint show that the sharpness and magnitude of SST and air-sea flux gradients on scales of tens of kilometers are likely underestimated with microwave satellite observations or coarse resolution models. This finding highlights the importance of using high resolution (<10 km) ocean and atmospheric measurements in air-sea flux studies and models in regions where ocean submesoscale variability exists. Calculating fluxes from lower resolution remote sensing observations will not capture small-scale gradients in fluxes or their components and may not resolve the aggregate influence of small-scale features on larger-scale air-sea fluxes, weather, ocean dynamics, or climate. Spatial gradients in fluxes and their thermodynamic components were significant in the northwestern tropical Atlantic trade wind region even though SST fronts are relatively less common and weaker here compared to other regions (Figure 1 of Mauzole, 2022). These results may be representative of other tropical trade wind regions, which cover a significant portion of the earth. The spatial variability of air-sea fluxes is likely larger or may behave differently in areas with stronger SST fronts and/or different atmospheric patterns, such as coastal regions, across tropical instability waves, near strong boundary currents, and at higher latitudes.

Data Availability Statement

SWIFT and Wave Glider data are available through NOAA National Centers for Environmental Information (NCEI) at https://doi.org/10.25921/s5d7-tc07 and https://doi.org/10.25921/dvys-1f29 (Thomson et al., 2021a, 2021b). Observations from the NOAA Ship *Ronald H. Brown* are also available through NOAA

NCEI at https://doi.org/10.25921/etxb-ht19 (Thompson et al., 2021). Satellite SST data are available through NASA PO.DAAC at https://doi.org/10.5067/GHOST-4FK01.

References

Banner, M. L., & Morison, R. P. (2010). Refined source terms in wind wave models with explicit wave breaking prediction. Part I: Model framework and validation against field data. *Ocean Modelling*, *33*(1–2), 177–189. https://doi.org/10.1016/j.ocemod.2010.01.002

Bishop, S. P., Small, R. J., Bryan, F. O., & Tomas, R. A. (2017). Scale dependence of midlatitude air–sea interaction. *Journal of Climate*, *30*(20), 8207–8221. https://doi.org/10.1175/JCLI-D-17-0159.1

Bryan, F. O., Tomas, R., Dennis, J. M., Chelton, D. B., Loeb, N. G., & McClean, J. L. (2010). Frontal scale air–sea interaction in high-resolution coupled climate models. *Journal of Climate*, *23*(23), 6277–6291. https://doi.org/10.1175/2010JCLI3665.1

Businger, J., & Shaw, W. (1984). The response of the marine boundary layer to mesoscale variations in sea-surface temperature. *Dynamics of Atmospheres and Oceans*, *8*(3–4), 267–281. https://doi.org/10.1016/0377-0265(84)90012-5

Capet, X., McWilliams, J. C., Molemaker, M. J., & Shchepetkin, A. F. (2008). Mesoscale to submesoscale transition in the California current system. Part I: Flow structure, eddy flux, and observational tests. *Journal of Physical Oceanography*, *38*(1), 29–43. https://doi.org/10.1175/2007JPO3671.1

Chelton, D. B., Schlax, M. G., Freilich, M. H., & Milliff, R. F. (2004). Satellite measurements reveal persistent small-scale features in ocean winds. *Science*, *303*(5660), 978–983. https://doi.org/10.1126/science.1091901

Chelton, D. B., & Xie, S.-P. (2010). Coupled ocean-atmosphere interaction at oceanic mesoscales. *Oceanography*, *23*(4), 52–69. https://doi.org/10.5670/oceanog.2010.05

de Szoeke, S. P., Skyllingstad, E. D., Zuidema, P., & Chandra, A. S. (2017). Cold pools and their influence on the tropical marine boundary layer. *Journal of the Atmospheric Sciences*, *74*(4), 1149–1168. https://doi.org/10.1175/JAS-D-16-0264.1

Dellaripa, E. M. R., & Maloney, E. D. (2015). Analysis of MJO wind-flux feedbacks in the Indian Ocean using RAMA buoy observations. *Journal of the Meteorological Society of Japan. Ser. II*, *93*(0), 1–20. https://doi.org/10.2151/jmsj.2015-021

DeMott, C. A., Benedict, J. J., Klingaman, N. P., Woolnough, S. J., & Randall, D. A. (2016). Diagnosing ocean feedbacks to the MJO: SST-modulated surface fluxes and the moist static energy budget. *Journal of Geophysical Research: Atmospheres*, *121*(14), 8350–8373. https://doi.org/10.1002/2016JD025098

Edson, J. B., Jampana, V., Weller, R. A., Bigorre, S. P., Plueddemann, A. J., Fairall, C. W., et al. (2013). On the exchange of momentum over the open ocean. *Journal of Physical Oceanography*, *43*(8), 1589–1610. https://doi.org/10.1175/JPO-D-12-0173.1

Fairall, C. W., Bradley, E. F., Godfrey, J. S., Wick, G. A., Edson, J. B., & Young, G. S. (1996). Cool-skin and warm-layer effects on sea surface temperature. *Journal of Geophysical Research*, *101*(C1), 1295–1308. https://doi.org/10.1029/95JC03190

Fairall, C. W., Bradley, E. F., Hare, J., Grachev, A. A., & Edson, J. B. (2003). Bulk parameterization of air–sea fluxes: Updates and verification for the COARE algorithm. *Journal of Climate*, *16*(4), 571–591. https://doi.org/10.1175/1520-0442(2003)016<0571BPOASF>2.0.CO;2

Fairall, C. W., Bradley, E. F., Rogers, D. P., Edson, J. B., & Young, G. S. (1996). Bulk parameterization of air-sea fluxes for tropical ocean-global atmosphere coupled-ocean atmosphere response experiment. *Journal of Geophysical Research*, *101*(C2), 3747–3764. https://doi.org/10.1029/95JC03205

Ffield, A. (2005). North Brazil current rings viewed by TRMM microwave imager SST and the influence of the Amazon Plume. *Deep Sea Research Part I: Oceanographic Research Papers*, *52*(1), 137–160. https://doi.org/10.1016/j.dsr.2004.05.013

Fratantoni, D. M., & Glickson, D. A. (2002). North Brazil Current ring generation and evolution observed with SeaWiFS. *Journal of Physical Oceanography*, *32*(3), 1058–1074. https://doi.org/10.1175/1520-0485(2002)032<1058:NBCRGA>2.0.CO;2

Fratantoni, D. M., & Richardson, P. L. (2006). The evolution and demise of North Brazil Current rings. *Journal of Physical Oceanography*, *36*(7), 1241–1264. https://doi.org/10.1175/JPO2907.1

Friehe, C., Shaw, W., Rogers, D., Davidson, K., Large, W., Stage, S., et al. (1991). Air-sea fluxes and surface layer turbulence around a sea surface temperature front. *Journal of Geophysical Research*, *96*(C5), 8593–8609. https://doi.org/10.1029/90JC02062

Gao, Y., Klingaman, N. P., DeMott, C. A., & Hsu, P.-C. (2019). Diagnosing ocean feedbacks to the BSISO: SST-modulated surface fluxes and the moist static energy budget. *Journal of Geophysical Research: Atmospheres*, *124*(1), 146–170. https://doi.org/10.1029/2018JD029303

Gaube, P., Chelton, D. B., Samelson, R. M., Schlax, M. G., & O'Neill, L. W. (2015). Satellite observations of mesoscale eddy-induced Ekman pumping. *Journal of Physical Oceanography*, *45*(1), 104–132. https://doi.org/10.1175/JPO-D-14-0032.1

Hayes, S., McPhaden, M., & Wallace, J. (1989). The influence of sea-surface temperature on surface wind in the eastern equatorial Pacific: Weekly to monthly variability. *Journal of Climate*, *2*(12), 1500–1506. https://doi.org/10.1175/1520-0442(1989)002<1500:TIOSST>2.0.CO;2

Hine, R., Willcox, S., Hine, G., & Richardson, T. (2009). The wave glider: A wave-powered autonomous marine vehicle. In *Oceans 2009* (pp.1–6). https://doi.org/10.23919/OCEANS.2009.5422129

Iyer, S., Thomson, J., Thompson, E., & Drushka, K. (2022). Variations in wave slope and momentum flux from wave-current interactions in the tropical trade winds. *Journal of Geophysical Research: Oceans*, *127*(3), e2021JC018003. https://doi.org/10.1029/2021JC018003

Jaimes, B., Shay, L. K., & Uhlhorn, E. W. (2015). Enthalpy and momentum fluxes during Hurricane Earl relative to underlying ocean features. *Monthly Weather Review*, *143*(1), 111–131. https://doi.org/10.1175/MWR-D-13-00277.1

Johnson, R. H., Ciesielski, P. E., & Cotturone, J. A. (2001). Multiscale variability of the atmospheric mixed layer over the Western Pacific warm pool. *Journal of the Atmospheric Sciences*, *58*(18), 2729–2750. https://doi.org/10.1175/1520-0469(2001)058<2729:mvotam>2.0.co;2

Kelly, K. A., Small, R. J., Samelson, R., Qiu, B., Joyce, T. M., Kwon, Y.-O., & Cronin, M. F. (2010). Western boundary currents and frontal air–sea interaction: Gulf Stream and Kuroshio extension. *Journal of Climate*, *23*(21), 5644–5667. https://doi.org/10.1175/2010JCLI3346.1

Kwon, Y.-O., Alexander, M. A., Bond, N. A., Frankignoul, C., Nakamura, H., Qiu, B., & Thompson, L. A. (2010). Role of the Gulf Stream and Kuroshio–Oyashio systems in large-scale atmosphere–ocean interaction: A review. *Journal of Climate*, *23*(12), 3249–3281. https://doi.org/10.1175/2010JCLI3343.1

Lambaerts, J., Lapeyre, G., Plougonven, R., & Klein, P. (2013). Atmospheric response to sea surface temperature mesoscale structures. *Journal of Geophysical Research: Atmospheres*, *118*(17), 9611–9621. https://doi.org/10.1002/jgrd.50769

Laurindo, L. C., Small, R. J., Thompson, L., Siqueira, L., Bryan, F. O., Chang, P., et al. (2022). Role of ocean and atmosphere variability in scale-dependent thermodynamic air-sea interactions. *Journal of Geophysical Research: Oceans*, *127*(7), e2021JC018340. https://doi.org/10.1029/2021JC018340

Lindzen, R. S., & Nigam, S. (1987). On the role of sea surface temperature gradients in forcing low-level winds and convergence in the tropics. *Journal of the Atmospheric Sciences*, *44*(17), 2418–2436. https://doi.org/10.1175/1520-0469(1987)044<2418:OTROSS>2.0.CO;2

Mauzole, Y. (2022). Objective delineation of persistent SST fronts based on global satellite observations. *Remote Sensing of Environment*, *269*, 112798. https://doi.org/10.1016/j.rse.2021.112798

Minobe, S., Kuwano-Yoshida, A., Komori, N., Xie, S.-P., & Small, R. J. (2008). Influence of the Gulf Stream on the troposphere. *Nature*, *452*(7184), 206–209. https://doi.org/10.1038/nature06690

O'Neill, L. W., Chelton, D. B., Esbensen, S. K., & Wentz, F. J. (2005). High-resolution satellite measurements of the atmospheric boundary layer response to SST variations along the Agulhas return current. *Journal of Climate*, *18*(14), 2706–2723. https://doi.org/10.1175/JCLI3415.1

Paulson, C., & Simpson, J. (1981). The temperature difference across the cool skin of the ocean. *Journal of Geophysical Research*, *86*(C11), 11044–11054. https://doi.org/10.1029/JC086iC11p11044

Quinn, P. K., Thompson, E. J., Coffman, D. J., Baidar, S., Bariteau, L., Bates, T. S., et al. (2021). Measurements from the RV Ronald H. Brown and related platforms as part of the Atlantic Tradewind Ocean-atmosphere mesoscale interaction campaign (ATOMIC). *Earth System Science Data*, *13*(4), 1759–1790. https://doi.org/10.5194/essd-13-1759-2021

Redelsperger, J.-L., Bouin, M.-N., Pianezze, J., Garnier, V., & Marié, L. (2019). Impact of a sharp, small-scale SST front on the marine atmospheric boundary layer on the Iroise Sea: Analysis from a hectometric simulation. *Quarterly Journal of the Royal Meteorological Society*, *145*(725), 3692–3714. https://doi.org/10.1002/qj.3650

Samelson, R., O'Neill, L., Chelton, D., Skyllingstad, E., Barbour, P., & Durski, S. (2020). Surface stress and atmospheric boundary layer response to mesoscale SST structure in coupled simulations of the northern California current system. *Monthly Weather Review*, *148*(1), 259–287. https://doi.org/10.1175/MWR-D-19-0200.1

Samelson, R., Skyllingstad, E., Chelton, D., Esbensen, S., O'Neill, L., & Thum, N. (2006). On the coupling of wind stress and sea surface temperature. *Journal of Climate*, *19*(8), 1557–1566. https://doi.org/10.1175/JCLI3682.1

Seo, H. (2017). Distinct influence of air–sea interactions mediated by mesoscale sea surface temperature and surface current in the Arabian Sea. *Journal of Climate*, *30*(20), 8061–8080. https://doi.org/10.1175/JCLI-D-16-0834.1

Seo, H., Jochum, M., Murtugudde, R., & Miller, A. J. (2006). Effect of ocean mesoscale variability on the mean state of tropical Atlantic climate. *Geophysical Research Letters*, *33*(9), L09606. https://doi.org/10.1029/2005GL025651

Seo, H., Jochum, M., Murtugudde, R., Miller, A. J., & Roads, J. O. (2007). Feedback of tropical instability-wave-induced atmospheric variability onto the ocean. *Journal of Climate*, *20*(23), 5842–5855. https://doi.org/10.1175/JCLI4330.1

Shao, M., Ortiz-Suslow, D. G., Haus, B. K., Lund, B., Williams, N. J., Özgökmen, T. M., et al. (2019). The variability of winds and fluxes observed near submesoscale fronts. *Journal of Geophysical Research: Oceans*, *124*(11), 7756–7780. https://doi.org/10.1029/2019JC015236

Shinoda, T., Hendon, H. H., & Glick, J. (1998). Intraseasonal variability of surface fluxes and sea surface temperature in the tropical Western Pacific and Indian Oceans. *Journal of Climate*, *11*(7), 1685–1702. https://doi.org/10.1175/1520-0442(1998)011<1685:IVOSFA>2.0.CO;2

Small, R., de Szoeke, S. P., Xie, S., O'neill, L., Seo, H., Song, Q., et al. (2008). Air–sea interaction over ocean fronts and eddies. *Dynamics of Atmospheres and Oceans*, *45*(3–4), 274–319. https://doi.org/10.1016/j.dynatmoce.2008.01.001

Small, R. J., Bacmeister, J., Bailey, D., Baker, A., Bishop, S., Bryan, F., et al. (2014). A new synoptic scale resolving global climate simulation using the community Earth system model. *Journal of Advances in Modeling Earth Systems*, *6*(4), 1065–1094. https://doi.org/10.1002/2014MS000363

Small, R. J., Bryan, F. O., Bishop, S. P., & Tomas, R. A. (2019). Air–sea turbulent heat fluxes in climate models and observational analyses: What drives their variability? *Journal of Climate*, *32*(8), 2397–2421. https://doi.org/10.1175/JCLI-D-18-0576.1

Stevens, B., Bony, S., Farrell, D., Ament, F., Blyth, A., Fairall, C., et al. (2021). EUREC4A. Earth System Science Data Discussions (pp. 1–78). https://doi.org/10.5194/essd-2021-18

Strobach, E., Klein, P., Molod, A., Fahad, A. A., Trayanov, A., Menemenlis, D., & Torres, H. (2022). Local air-sea interactions at ocean mesoscale and submesoscale in a Western boundary current. *Geophysical Research Letters*, *49*(7), e2021GL097003. https://doi.org/10.1029/2021GL097003

Stull, R. B. (1988). *An introduction to boundary layer meteorology* (Vol. 13). Springer Science & Business Media.

Su, Z., Wang, J., Klein, P., Thompson, A. F., & Menemenlis, D. (2018). Ocean submesoscales as a key component of the global heat budget. *Nature Communications*, *9*(1), 1–8. https://doi.org/10.1038/s41467-018-02983-w

Sullivan, P. P., McWilliams, J. C., Weil, J. C., Patton, E. G., & Fernando, H. J. (2020). Marine boundary layers above heterogeneous SST: Across-front winds. *Journal of the Atmospheric Sciences*, *77*(12), 4251–4275. https://doi.org/10.1175/JAS-D-20-0062.1

Sullivan, P. P., McWilliams, J. C., Weil, J. C., Patton, E. G., & Fernando, H. J. (2021). Marine boundary layers above heterogeneous SST: Along-front winds. *Journal of the Atmospheric Sciences*, *78*(10), 3297–3315. https://doi.org/10.1175/JAS-D-21-0072.1

Sweet, W., Fett, R., Kerling, J., & La Violette, P. (1981). Air-sea interaction effects in the lower troposphere across the north wall of the Gulf Stream. *Monthly Weather Review*, *109*(5), 1042–1052. https://doi.org/10.1175/1520-0493(1981)109<1042:ASIEIT>2.0.CO

Thompson, E., Fairall, C., Pezoa, S., & Bariteau, L. (2021). ATOMIC ship navigation, meteorology, seawater, fluxes: Near-surface meteorology, air-sea fluxes, surface ocean waves, and near surface ocean parameters (temperature, salinity, currents) and primary dataset of ship location and navigation estimated from in-situ and remote sensing instruments aboard NOAA Ship Ronald H. Brown in the North Atlantic Ocean, near Barbados: Atlantic Tradewind Ocean-Atmosphere Mesoscale Interaction Campaign 2020-01-09 to 2020-02-12 (NCEI Accession 0225427) [Dataset]. NOAA National Centers for Environmental Information. https://doi.org/10.25921/etxb-ht19

Thomson, J. (2012). Wave breaking dissipation observed with "SWIFT" drifters. *Journal of Atmospheric and Oceanic Technology*, *29*(12), 1866–1882. https://doi.org/10.1175/JTECH-D-12-00018.1

Thomson, J., Moulton, M., de Klerk, A., Talbert, J., Guerra, M., Kastner, S., et al. (2019). A new version of the SWIFT platform for waves, currents, and turbulence in the ocean surface layer. In *2019 IEEE/OES twelfth current, waves and turbulence measurement (CWTM)* (pp. 1–7). https://doi.org/10.1109/CWTM43797.2019.8955299

Thomson, J., Thompson, E., Iyer, S., Drushka, K., & de Klerk, A. (2021a). ATOMIC SWIFT drifters: Near-surface meteorology, air-sea fluxes, surface ocean waves, and near-surface ocean properties (turbulent dissipation rate, currents, temperature, salinity) estimated from in-situ and remote sensing instruments aboard six SWIFT drifters (Surface Wave Instrument Float with Tracking) launched and recovered from two different deployments from NOAA Ship Ronald H. Brown in the North Atlantic Ocean, near Barbados: Atlantic Tradewind Ocean-Atmosphere Mesoscale Interaction Campaign 2020-01-14 to 2020-02-11 (NCEI Accession 0225279) [Dataset]. NOAA National Centers for Environmental Information. https://doi.org/10.25921/s5d7-tc07

Thomson, J., Thompson, E., Iyer, S., Drushka, K., & de Klerk, A. (2021b). ATOMIC Wave Gliders: Near-surface meteorology, air-sea fluxes, surface ocean waves, and near-surface ocean parameters (currents, temperature, salinity) estimated from in-situ and remote sensing instruments aboard two Wave Gliders launched and recovered from NOAA Ship Ronald H. Brown in the North Atlantic Ocean, near Barbados: Atlantic Tradewind Ocean-Atmosphere Mesoscale Interaction Campaign 2020-01-09 to 2020-02-11 (NCEI Accession 0225336) [Dataset]. NOAA National Centers for Environmental Information. https://doi.org/10.25921/dvys-1f29

Thum, N., Esbensen, S. K., Chelton, D. B., & McPhaden, M. J. (2002). Air–sea heat exchange along the northern sea surface temperature front in the eastern tropical Pacific. *Journal of Climate*, *15*(23), 3361–3378. https://doi.org/10.1175/1520-0442(2002)015<3361:ASHEAT>2.0.CO;2

Thyng, K. M., Greene, C. A., Hetland, R. D., Zimmerle, H. M., & DiMarco, S. F. (2016). True colors of oceanography: Guidelines for effective and accurate colormap selection. *Oceanography*, *29*(3), 9–13. https://doi.org/10.5670/oceanog.2016.66

UK Met Office. (2005). *OSTIA L4 SST analysis. Version 2.0*. PO.DAAC. https://doi.org/10.5067/GHOST-4FK01

Wallace, J. M., Mitchell, T., & Deser, C. (1989). The influence of sea-surface temperature on surface wind in the eastern equatorial Pacific: Seasonal and interannual variability. *Journal of Climate*, *2*(12), 1492–1499. https://doi.org/10.1175/1520-0442(1989)002<1492:TIOSST>2.0.CO;2

Wenegrat, J., & Arthur, R. (2018). Response of the atmospheric boundary layer to submesoscale sea surface temperature fronts. *Geophysical Research Letters*, *45*(24), 13–505. https://doi.org/10.1029/2018GL081034

Wick, G. A., Jackson, D. L., & Castro, S. L. (2022). *Assessing the ability of satellites to resolve spatial sea surface temperature variability—the northwest tropical Atlantic ATOMIC region*. Remote Sensing of Environment.

Yokoi, S., Katsumata, M., & Yoneyama, K. (2014). Variability in surface meteorology and air-sea fluxes due to cumulus convective systems observed during CINDY/DYNAMO. *Journal of Geophysical Research: Atmospheres*, *119*(5), 2064–2078. https://doi.org/10.1002/2013JD020621

Yu, L. (2019). Global air–sea fluxes of heat, fresh water, and momentum: Energy budget closure and unanswered questions. *Annual Review of Marine Science*, *11*(1), 227–248. https://doi.org/10.1146/annurev-marine-010816-060704

Yu, L., & Weller, R. A. (2007). Objectively analyzed air–sea heat fluxes for the global ice-free oceans (1981–2005). *Bulletin of the American Meteorological Society*, *88*(4), 527–540. https://doi.org/10.1175/BAMS-88-4-527

Zhang, G. J., & McPhaden, M. J. (1995). The relationship between sea surface temperature and latent heat flux in the equatorial Pacific. *Journal of Climate*, *8*(3), 589–605. https://doi.org/10.1175/1520-0442(1995)008<0589:TRBSST>2.0.CO;2

Zuidema, P., Li, Z., Hill, R. J., Bariteau, L., Rilling, B., Fairall, C., et al. (2012). On trade wind cumulus cold pools. *Journal of the Atmospheric Sciences*, *69*(1), 258–280. https://doi.org/10.1175/JAS-D-11-0143.1